Chapter 3

Dynamical Properties of Hamiltonian Systems with Applications to Celestial Mechanics

Carles Simó

3.1 Introduction

Our goal is to study some properties of the *dynamics of the N-body problem*. As is well known, the *Newtonian model of N punctual masses*, $m_i, i = 1, \ldots, N$, located at $q_i(t) \in \mathbb{R}^d$, moving under their mutual gravitational attraction is described by the equations

$$\ddot{q}_i = \sum_{j=1, j\neq i}^{N} (q_j - q_i)/r_{i,j}^3, \quad r_{i,j}^2 = ||q_j - q_i||_2^2, \quad i = 1, \ldots, N. \tag{3.1}$$

The system has several *first integrals*. The centre of mass ones, in a suitable reference moving linearly with constant velocity, are $\sum_{i=1}^N m_i q_i = 0$, $\sum_{i=1}^N p_i = 0$, where the related momenta are defined as $p_i = m_i \dot{q}_i$. Furthermore, defining the kinetic energy as $T(p) = \sum_{i=1}^N ||p_i||_2^2/m_i$ and the potential one as $U(q) = \sum_{1\leq i<j\leq N} m_i m_j / r_{i,j}$, one has the energy integral $T(p) - U(q) = H(q,p) = h$. The total angular momentum $\sum_{i=1}^N m_i q_i \wedge \dot{q}_i$ is another first integral. In general, no more first integrals exist. Of course, q and p above refer to the vectors in $\mathbb{R}^{Nd}$ which contain all the components of positions and momenta. System (3.1) can be put in *Hamiltonian formulation*: $\dot{q}_i = \partial H/\partial p_i$, $\dot{p}_i = -\partial H/\partial q_i$. The pairs (q_i, p_i)

J. Llibre et al., *Central Configurations, Periodic Orbits, and Hamiltonian Systems*,
Advanced Courses in Mathematics - CRM Barcelona, DOI 10.1007/978-3-0348-0933-7_3

are canonically conjugated. In the present case, the Hamiltonian has Nd degrees of freedom (d.o.f.), despite the fact that the centre of mass integrals reduces them to $(N-1)d$, and the angular momentum gives additional reduction. For applications we shall consider the cases $d = 2$ and $d = 3$. The equations are analytic except on the collision set, when at least one of the values of $r_{i,j}$ equals zero.

In many problems it is interesting to consider that some of the bodies have a negligible mass. They are influenced by massive bodies but have no action on them. These are the *restricted* N-body problems.

The N-body problem belongs to the general class of Hamiltonian systems. In these systems and in all kinds of dynamical systems, the ultimate goal is *to describe the main mechanisms leading to a fairly global description of the dynamics*, how it depends on parameters and, if it is possible to act on the system (either with additional forces or by changing parameters), how to have some control on the behaviour of the system. In the present case we shall be interested in *conservative systems*, either in the continuous version described by a Hamiltonian or in the discrete version. Next we make some comments on the passage from continuous systems to discrete ones and vice-versa.

3.1.1 Continuous and discrete conservative systems

The associated discrete version is given by *symplectic maps*: $F\colon (x, y) \to (X, Y)$, where $X = F_1(x, y)$, $Y = F_2(x, y)$, with x, y, X, Y belonging to some set in $\mathbb{R}^d$ and such that the 2-form $dx \wedge dy = \sum_{i=1}^{d} dx_i \wedge dy_i$ is preserved: $dX \wedge dY = dx \wedge dy$. We can replace working in $\mathbb{R}^d \times \mathbb{R}^d$ by a formulation in symplectic manifolds but, to have a simpler presentation, we prefer to work explicitly using coordinates and refraining from extensions.

It is a simple matter to obtain discrete maps from a flow led by $\dot{x} = f(x)$, where f is a vector field (v.f.) in some open set U of $\mathbb{R}^n$. Assume Σ is a hypersurface, given as points $x \in U$ such that $g(x) = 0$, where $g\colon U \to \mathbb{R}$. We require that it satisfies the *transversality condition*. We say that Σ is transversal to the v.f. if the scalar product $(f, \nabla g)$ is different from zero in Σ. The geometrical meaning is clear: the flow of f (that we shall denote as φ_t^f or simply as φ_t) crosses transversally the section Σ. In many examples one simply takes as g one of the coordinates (either equal to zero or to a constant). In that case, Σ is usually not the full coordinate hyperplane, but the part of it satisfying the transversality condition. Then, given a point $Q \in \Sigma$ we define a map, the so-called *Poincaré map* $\mathcal{P}$, as the first return of Q to Σ: $\varphi_{t(Q)}(Q) \in \Sigma$ with a minimal value of $t(Q) > 0$. Note that, eventually, some Q can never return to Σ for any $t > 0$. This implies that Σ has to be reduced to a suitable subset. We also note that the return time $t(Q)$ depends on the starting point. We denote as $\mathcal{P}(Q) := \varphi_{t(Q)}(Q)$ the image of Q under the Poincaré map $\mathcal{P}$.

In the case of a Hamiltonian H with m d.o.f. (hence x has dimension $2m$) fixing a transversal section Σ and the level of energy h, the Poincaré map associated

to Σ defines a map in $\Sigma \cap H^{-1}(h)$, of even dimension $2(m-1)$. This map is symplectic.

Given a discrete map $x \to F(x)$ in $V \subset \mathbb{R}^n$, there is also a simple way to produce a v.f. such that it has, as associated Poincaré map, the initial map, provided F is close to the identity, say $F(x) = x + \varepsilon G(x)$ with ε small enough (see later). For concreteness we shall assume that G is a real analytic function. We want to define a non-autonomous periodic v.f. of period 1 in t. Let us consider, for instance, and for a given $k > 1$, the function $\psi_k(t) = c \int_0^t s^k(1-s)^k \, ds$, where the constant c is selected to have $\psi_k(1) = 1$. Then we define the flow starting at the point x after a time $t \in [0,1]$ as $\varphi_t(x) = x + \varepsilon \psi_k(t) G(x)$, that is, we are using an Hermite-like interpolation, because $\psi_k^j(0) = 0$ for $j = 0, \ldots, k$, $\psi_k(1) = 1$, and $\psi_k^j(1) = 0$ for $j = 1, \ldots, k$. Other interpolations can also be used. For other values of t it is defined by periodicity: $\varphi_t(x) = \varphi_{(t)}(x)$ where $(t) = t - [t]$, being $[t]$ the largest integer less than or equal to t. Clearly $\varphi_0(x) = x$, $\varphi_1(x) = F(x)$. Now we should define the v.f. at (y, τ) for $\tau \in [0,1]$. To this end we look for z such that $\varphi_\tau(z) = y$. It follows immediately, from the implicit function theorem, that a solution exists if $|| \operatorname{Id} + \varepsilon DG||_\infty > 0$. Finally the v.f. is $f(y,\tau) = \varepsilon \frac{d\psi_k}{dt}(\tau) G(z)$.

We note that this is a slow v.f., having the parameter ε as a factor. It is usually referred to as the *suspension* of the map F. We can consider if it is possible to approximate it by an autonomous v.f. This follows from a general theorem on averaging, that we present in a wider context: the case of v.f. depending on time in a quasiperiodic way.

Theorem 3.1.1. *Let*

$$\dot{z} = \varepsilon f(z, \theta, \varepsilon), \tag{3.2}$$

where f is analytic in (z,θ) for $z \in \Omega \subset \mathbb{C}^n$, $\Omega = D + \Delta$, a Δ-neighbourhood of D in $\mathbb{C}^n$, D a compact in $\mathbb{R}^n$, and $\theta \in \mathbb{T}^p + \Delta$, $p \geq 2$, where $\mathbb{T}^p$ is a p-dimensional torus. Assume f in (3.2) *is bounded in ε for $|\varepsilon| \leq \varepsilon_0$ and $\theta = \omega t$, where $\omega \in \mathbb{R}^n$ is a vector of frequencies satisfying the Diophantine condition* (DC)

$$|(k, \omega)| \geq b|k|^{-\tau}, \quad \forall k \in \mathbb{Z}^p \setminus \{0\}, \tag{3.3}$$

where $b > 0$, $\tau > p-1$ and $|k| = \sum_{i=1}^p |k_i|$. Then, if ε_0 is small enough, for a fixed ε with $|\varepsilon| \leq \varepsilon_0$, there exists a change of variables $z = h(w, \theta, \varepsilon)$, analytic in (w, θ) for $w \in D + \Delta/2$, $\theta \in \mathbb{T}^p + \Delta/2$, such that the new equation is $\dot{w} = \varepsilon(g(w,\varepsilon) + r(w,\theta,\varepsilon))$ and the remainder satisfies an exponentially small bound

$$|r|_{\Delta/2} < c_1 \exp(-c_2/\varepsilon^{c_3}), \tag{3.4}$$

where c_1, $c_2 > 0$, $c_3 = 1/(\tau+1)$. The constants c_1, c_2 depend only on $|f|_\Delta$, the dimensions and the constants in (3.3). *Furthermore, $|g|_{\Delta/2} < 2|f|_\Delta$. Here $|f|_\Delta$ denotes the sup norm of f in $D + \Delta$, $\mathbb{T}^p + \Delta$ for the fixed value of ε.*

Remark 3.1.2. (i) In the periodic case (it would be $p = 1, \tau = 0$), there is no need of analyticity with respect to t; just integrable is enough. Then $c_3 = 1$, see [36].

(ii) The optimal number of averaging steps (i.e., up to which order in ε one should cancel the quasiperiodic dependence) is $\approx \varepsilon^{-c_3}$.

(iii) If f is a Hamiltonian v.f., the change to w can be made canonical. Hence, the averaged system, skipping the remainder r, is also Hamiltonian, see [51].

(iv) If f has been obtained by suspension of a map F, we can produce an autonomous v.f., like g, which interpolates F except by exponentially small terms.

The basic idea of the proof is to obtain the change $z = h(w, \theta, \varepsilon)$ by means of *sequence of changes*. This methodology is common to many topics in dynamical systems. First we try to cancel the *purely quasiperiodic* terms in f, that is, the terms in $\tilde{f} = f - \bar{f}$, where $\bar{f}$ denotes the average with respect to θ. Writing the suitable condition for the change, one has to solve a PDE to obtain the quasiperiodic coefficients in this first change. To solve it with control on how the coefficients of the change behave is where the *analyticity with respect to* θ and the DC (3.3) play their roles. In the periodic case one has to do just an integration, and this is why to be integrable in t is enough in that case.

Once the terms in $\tilde{f}$ have been skipped, one has to check the contribution that the change makes in ε^2. Here is where the *analyticity with respect to* z plays a role, to bound the derivatives in a slightly smaller strip, passing from half width Δ to Δ_1. Then we proceed to cancel the purely quasiperiodic terms which appear with ε^2 as factor, and so on, to cancel the non-autonomous terms in ε^k, $k = 3, \ldots$ At every step, to be able to bound the contributions made by the change to higher order in ε, one has to reduce the size of the analyticity domain, introducing a decreasing sequence for the half widths of the successive domains $\Delta_2 > \cdots > \Delta_k > \cdots$.

After every change one has a bound on the remainder. If for a given ε we do too many changes, as we want to keep an analyticity domain of positive half width, the differences $\Delta_{k-1} - \Delta_k$ are small. This implies bad estimates for the derivatives and an increase on the size of the remainder. This is why, for every ε, there is an optimal order. Simpler estimates give then the bound in (3.4). See [41] for details and examples.

These kind of bounds on remainders are relevant to bound errors on approximations done, for instance, with normal forms (see Subsection 3.3.2). The variables can be scaled in the domain of interest and the role of ε is played by the size of the domain.

Finally we stress that the passage from flows to maps and vice-versa, when the map or some power of it is close enough to the identity, allows a more complete understanding and representation of key phenomena.

In what follows we shall consider that all v.f. and maps are in the analytic category.

3.1.2 Comments on the contents

Setting aside the two-body problem and subclasses with some special symmetry, the simplest N-body problem is the planar circular restricted three-body problem which has two d.o.f. (see Section 3.4). The next simplest problem can be the planar general three-body problem. Even restricting to a fixed value of the angular momentum it has three d.o.f. The dimension can be reduced by fixing energy and using a Poincaré section. In the first case we obtain symplectic 2D maps, easy to visualize. In the second case we have symplectic 4D maps, not so easy to visualize. There are key objects of codimension one (see Subsection 3.3.4) and homoclinic/heteroclinic phenomena due to the intersection of two objects of dimension two in dimension four. The invariant tori (see Subsection 3.3.3) do not separate the phase space, and slow escape from points as close as we like to invariant tori (Arnold diffusion or general diffusion, see Subsection 3.3.5), avoiding a large set of nearby tori, can occur.

For these reasons we devote Section 3.2 to introducing several simple but paradigmatic examples in the 2D case, with the hope that they will make it easier to grasp the main ideas in higher dimension. See also slides (B) for several examples with low dimensional conservative systems.

Section 3.3 is devoted to presenting some general theoretical results. But it is also relevant to see how to use the ideas of the proofs in concrete examples. In many cases, effective computation is based on implementation of the proof, either by symbolical or numerical methods or, quite frequently, by a combination of both.

Finally Section 3.4 presents some applications to Celestial Mechanics, with a variety of goals.

Concerning references, most of the basic results can be found in classical standard books. A few of them appear in the list of references, and no explicit mention to them is made in the text. Some references to concrete topics are scattered throughout the text and they are given at the end of these notes. The reader can also, at the end of the references, look at the list of slides of several talks given in the past and that, in turn, refer to some animations.

3.2 Low dimension: same key examples of 2D symplectic maps to see the kind of phenomena to face

Invariance of $dx \wedge dy$ in dimension 2 is equivalent to area preservation. We shall denote as APM the area preserving maps. The simplest non-trivial APM which come to mind are the quadratic ones: $x, y \in \mathbb{R}$ and F_1, F_2 are polynomials of degree

two. These maps were widely studied by M. Hénon [20]. See also slides (E) and slides (G). They are relevant because:

(i) the number of parameters can be reduced to only one, and they have a very simple geometrical interpretation;

(ii) they appear in a natural way as a very good approximation in some parts of $\mathbb{R}^2$ when we consider arbitrary APM; in particular when we study Poincaré maps of Hamiltonian systems with two d.o.f.;

(iii) the following problems can all be understood thanks to our knowledge of the quadratic case: (a) the existence of invariant curves diffeomorphic to $\mathbb{S}^1$; (b) the role of the invariant manifolds of hyperbolic fixed or periodic points and how they lead to the existence of chaos; and (c) the geometrical mechanisms leading to the destruction of invariant curves.

We shall illustrate some of these features in this section.

3.2.1 The Hénon map

In the initial formulation the map (except in some degenerate cases) can be written, thanks to the APM character, shift of origin and scaling, as $F\colon (x, y) \to (1 - ax^2 + y, -x)$. Hence, this family of maps depends on a single parameter a. The geometric interpretation is simple: it is the composition of the map $(x, y) \to (x, y + 1 - ax^2)$ (one of the so-called de Jonquières maps) and a rotation of angle $-\pi/2$. Figure 3.1 shows, for $a = -1/2$, the square $[-3, 3]^2$ (in red), the first image (in green) and part of the next two images (in blue and magenta, respectively). One can ask whether all points will escape for future iterations. To give an answer to this question, we plot in black the set of points which remain bounded for all iterations and the selected value of a.

However, we shall use another representation of that map, see [52], given by

$$F_c \begin{pmatrix} x \\ y \end{pmatrix} \to \begin{pmatrix} x + 2y + \frac{c}{2}(1 - (x + y)^2) \\ y + \frac{c}{2}(1 - (x + y)^2) \end{pmatrix}, \tag{3.5}$$

which depends on c that can be assumed to be positive. It has two fixed points: H at $(-1, 0)$, hyperbolic $\forall c > 0$, and $E = (1, 0)$, elliptic for $0 < c < 2$ and hyperbolic with reflection for $c > 2$. The reversor $S(x, y) = (x, -y)$ allows us to obtain $F_c^{-1} = SF_cS$.

Doing the change of scale $(\xi, \eta) = (x, 2y/\sqrt{c})$ one obtains a map $\sqrt{c}$-close to the identity. According to Section 3.1 it can be approximated by the time-$\sqrt{c}$ flow of the v.f. $d\xi/dt = \eta$, $d\eta/dt = 1 - \xi^2$, with Hamiltonian $K(\xi, \eta) = \eta^2/2 - \xi + \xi^3/3$. It is, of course, a trivial matter to improve K to any power of $\sqrt{c}$. This v.f. has the same fixed points as F_c and a separatrix on the level $K = 2/3$.

Next we show iterates of some initial points under F_c for $c = 0.2$ and $c = 0.762$, see Figure 3.2.

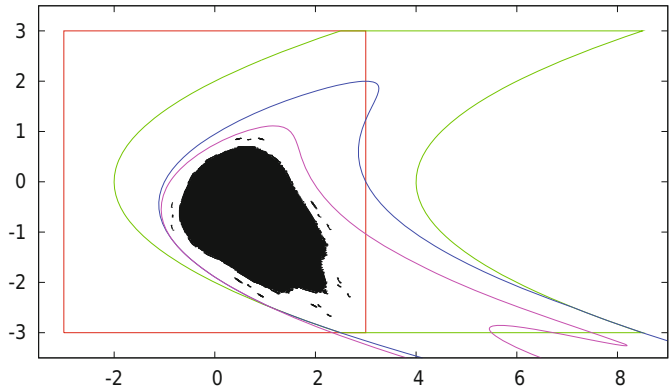

Figure 3.1: The square $[-3, 3]^2$ (in red) and the first three images of it under the Hénon map with $a = -0.5$, shown in green, blue and magenta, respectively. The last two have parts outside the frame shown here. In black we display the invariant set of points which remain bounded under all iterations.

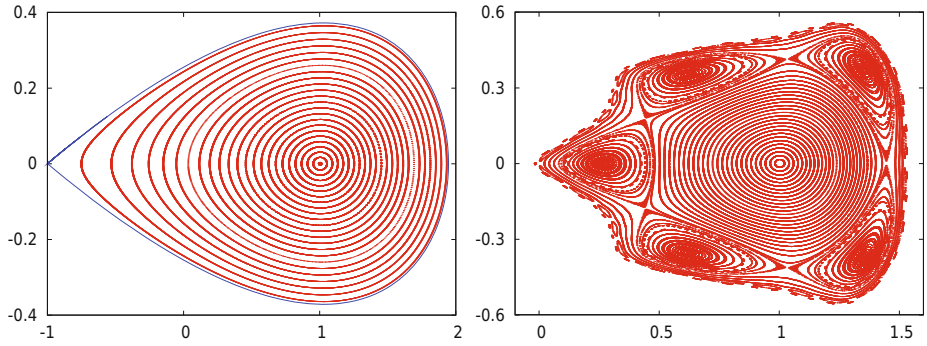

Figure 3.2: Some iterates under F_c. *Left:* for $c = 0.2$. *Right:* for $c = 0.762$. We have taken initial points on $y = 0$ and plotted 5,000 iterates of each one after a transient of 10^6 iterates. Points outside the displayed domain escape to infinity close to the left branch of W^u_H. When looking at the figure in the electronic version it is suggested to magnify the right plot to see the details. The same applies to several other plots in the next figures, without explicit mention.

An important characteristic of points whose orbit is an invariant curve (IC) is the *rotation number* ρ. It measures the average value of the fraction of revolution that the point turns in each iterate. We can look at the curves around the elliptic point E in previous plots and take polar coordinates. Let θ_k be the angle of the k-th iterate, but considered in the lift $\mathbb{R}$ instead of $\mathbb{S}$. Note that in this example

the points turn clockwise. Then, we define

$$\rho = \frac{1}{2\pi} \lim_{k\to\infty} \frac{\theta_k}{k}. \tag{3.6}$$

It always exists and does not depend on the initial point on the curve.

On the left plot in Figure 3.2 one can see a pattern which looks like the phase portrait of a one d.o.f. Hamiltonian, with a foliation by periodic solutions and a separatrix in blue. It seems that, as in the case of one d.o.f. systems, the map is *integrable*. That is, there exists a non-constant function $C(x, y)$ preserved by the map: $C(F(x, y)) = C(x, y)$. In fact there is a Cantor set (of positive measure) of ICs with $\rho \notin \mathbb{Q}$, an infinite number of periodic orbits of elliptic and hyperbolic type and the right-hand sides of the manifolds of H do not coincide. What happens is that the differences with respect to the flow case are extremely small, in agreement with (3.4). We shall see details on this smallness in the part about invariant manifolds of Section 3.2.1.

The right-hand plot in Figure 3.2 displays a typical behaviour of a *not close to integrable APM*. Certainly there are many ICs (again a Cantor set) around the point E, but at some distance one can see big *period-5 islands* around elliptic periodic points of period 5, and one can guess the existence of period-5 hyperbolic points. Close to them there are *chaotic orbits*, still surrounded by some more ICs, (rotational, that is, they make the full turn around E) and, finally, some little islands before reaching a place where most of the points *escape*.

Some comments on invariant curves

The plots in Figure 3.2 raise several questions: (1) do ICs really exist for F_c? (2) what is the structure of the set of ICs? (3) how are they destroyed? (4) what happens after an IC's destruction?

First we introduce the so-called *twist maps*. These are integrable maps defined in some annular domain $r_d < r < r_u$, having a foliation by ICs, given by

$$T(r, \alpha) = (r, \alpha + a(r)), \tag{3.7}$$

and satisfying the *twist condition*

$$da(r)/dr \neq 0. \tag{3.8}$$

Of course, one can have the form (3.7) after a diffeomorphism. The curves can have a shape different from circles, like ellipses, to be star-shaped or not.

A key result is the *Moser twist theorem*.

Theorem 3.2.1. *Consider a perturbation $F_\varepsilon = T + \varepsilon P$ of a twist map T. Then, if we have an invariant curve of T which has Diophantine rotation number γ, this curve, with a small deformation, subsists for F_ε provided ε is sufficiently small.*

The Diophantine condition, in the present case, is like (3.3) with frequencies γ and 1: $|k_1\gamma + k_0| \geq b|k|^{-\tau}$, $\forall (k_1, k_0) \in \mathbb{Z}^2 \setminus \{0\}$, where $|k|$ denotes some norm of $k = (k_1, k_0)$.

Let us comment a little on the three conditions: (a) it must be a perturbation of a twist map T; (b) the rotation number γ must be Diophantine; and (c) it must be close enough to T, that is, ε must be small.

Assume that the Fourier representation of the IC of T which has $\rho = \gamma$ is $r(\alpha) = \sum_{j\in\mathbb{Z}} a_j \exp(\mathrm{i}\, j\alpha)$ in the present polar coordinates we are using (typically, for a given problem, the twist map will not be given in the form (3.7), and to put it explicitly in this form can be cumbersome). Let $r_\varepsilon(\alpha) = \sum_{j\in\mathbb{Z}} b_j \exp(\mathrm{i}\, j\alpha)$ be the representation of the desired IC, invariant under F_ε. The invariance condition is expressed, in (r, α), as $F_\varepsilon(r_\varepsilon(\alpha), \alpha) = (r_\varepsilon(\alpha + 2\pi\gamma), \alpha + 2\pi\gamma)$. It is clear that we can fix the origin of angles in an arbitrary way.

We try to pass from the coefficients a_j to b_j by making a sequence of changes (similar to the case of Theorem 3.1.1) such that, after the k-th change, one has an approximation of the IC under F_ε with $\rho = \gamma$ with an error $\mathcal{O}(\varepsilon^{2^k})$. That is, a Newton method in the space of Fourier series. The equation to be solved at each step is of the form $G(\alpha + 2\pi\gamma) - G(\alpha) = R(\alpha)$, the so-called *homological equation*, where $R(\alpha)$ is related to the error of the previous approximation and has zero average, a necessary condition in order to make it possible to solve the equation.

Using Fourier representations for G and R, say $G = \sum_{j\in\mathbb{Z}} g_j \exp(\mathrm{i}\, j\alpha)$ and $R = \sum_{j\in\mathbb{Z}} r_j \exp(\mathrm{i}\, j\alpha)$, $r_0 = 0$, it is straightforward to obtain $g_j = r_j/(\exp(\mathrm{i}\, j2\pi\gamma) - 1)$, $j \neq 0$. But, of course, if $j\gamma$ is close to an integer, the previous denominator is close to zero. This is known as the *small denominators problem*. The DC allows us to control the behaviour of the coefficients of G, so that if R is analytic in some complex strip around real values of α, G is also analytic (perhaps in a slightly narrower strip).

The problem is then that the error in the next approximation does not have zero average and we will not be able to solve the next homological equation. But this average can be canceled by modifying the initial independent term a_0 (or, equivalently, by selecting a proper value for g_0) and this is possible, thanks to the twist condition, by applying the implicit function theorem. It is convenient to express the twist condition as $d\rho/da_0 \neq 0$; that is, in terms of the average of the initial curve. Finally the smallness of ε is necessary to have convergence in the Newton procedure. Note that, for a fixed γ, the larger is the twist condition, the larger are the admissible values of ε.

In Section 3.3.3 we shall talk about generalizations to higher dimension, both for symplectic maps and for Hamiltonian flows. The key ideas for the proofs are the same.

Using *normal form* tools (see Section 3.3.2) it is easy to prove that, what seem to be ICs in Figure 3.2 are really ICs, at least close to the point E. Furthermore, it is clear that the structure of the set of ICs is Cantorian, because so is the structure of the set of Diophantine numbers for values of b, τ bounded from below, see (3.3).

It is interesting to see what happens when the twist condition is *not satisfied*. Figure 3.3 shows, for the map (3.5), with $c = 1.35$, the evolution of ρ as a function of x for initial points of the form $(x, 0)$. It is clear that ρ is only defined for ICs and periodic orbits (or islands) and, in the present case, it seems that this occurs for most of the initial values of x. One can prove that this behaviour, with a local minimum at $x = 1$ and a local maximum on each side, appears only for $c \in (c_1, c_2)$, $c_1 = 5/4$, $c_2 \approx 1.4123$. For $c \in (0, c_1)$ one has a local (in fact, global) maximum at $x = 1$ (the point E).

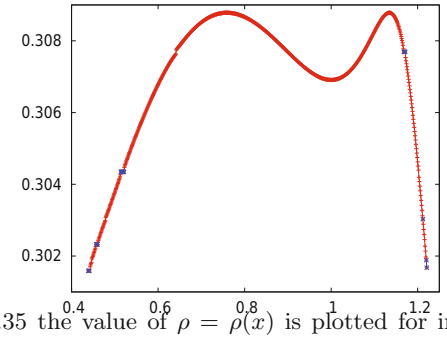

Figure 3.3: For $c = 1.35$ the value of $\rho = \rho(x)$ is plotted for initial points on $y = 0$. In blue the points with $\rho \in \mathbb{Q}$. Note that now, to the left or to the right of $x = 1$, the function ρ is no longer monotonous.

The twist condition is lost near the maxima. Let ρ_M be the value of ρ at a given maximum M. Assume that there exist rationals $p/q < \rho_M$ with q not too large. They give rise to the typical islands structure, with q islands on each family, on both sides of the IC with $\rho = \rho_M$ (or close to it). The interaction of these two families of islands, with $\rho = p/q$, gives rise to the so-called *meandering curves*, see [43], which cannot be written with the radius as a function of the angle seen from the point E. The curves have some folds (or meanders) but it is still possible to apply Moser's Theorem 3.2.1 to prove that they exist. Figure 3.4 shows an example of meandering ICs for $c = 1.3499$ and a magnification including some nearby orbits.

Some comments on invariant manifolds of hyperbolic points

Beyond the IC of an APM, there are other very important invariant objects which play a key role in dynamics (this is also true for more general maps and flows in any dimension, see Section 3.3.4). They are the *stable and unstable manifolds of the hyperbolic fixed or periodic points*. They can be seen as the non-linear generalisation of the invariant subspaces of the differential of the map at the fixed point. On the left-hand plot in Figure 3.2, for $c = 0.2$, the branches $W^{u,+}$ and $W^{s,-}$ (the ones which start to the right of $x = -1$) seem to be coincident, but they are not.

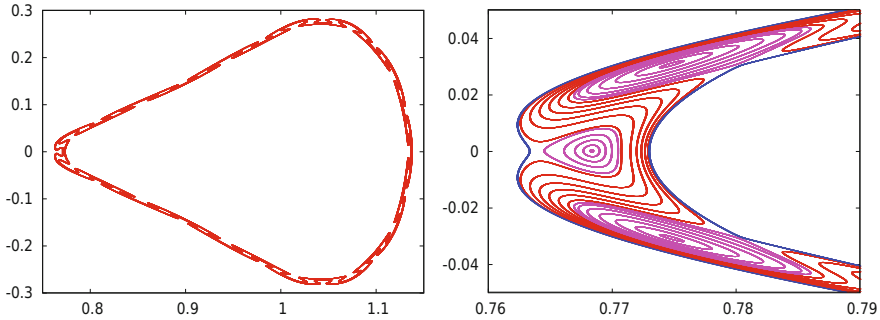

Figure 3.4: *Left:* We show a couple of orbits for $c = 1.3499$, sitting on a domain in which ρ passes through a maximum. These orbits are on invariant curves known as meanders. *Right:* A magnification of the left. Beyond different meanders in red, one can see two typical invariant curves (inner and outer) in blue and islands, in magenta, which belong to two different chains of islands of rotation number 4/13.

Figure 3.5, left, shows a magnification when they return to the vicinity of the point $(-1, 0)$, after going clockwise around E under F_c (red points), or counterclockwise under F_c^{-1} (blue points). We see tiny oscillations with a size $\mathcal{O}(10^{-3})$. The right-hand plot in Figure 3.5 shows the manifolds for $c = 0.77$ with large oscillations. The points in $W^u \cap W^s$ are known as *homoclinic points* (or biasymptotic points). Some of them, on $y = 0$, can be seen to the right of the plot. The successive nearby returns of the manifolds produce infinitely many homoclinic points. Depending on the location of a point with respect to a given homoclinic, after passing close to H under iteration by F_c, will follow close to the positive, $W^{u,+}$, or to the negative, $W^{u,-}$, branches of W^u. And similarly for the stable branches using F_c^{-1}.

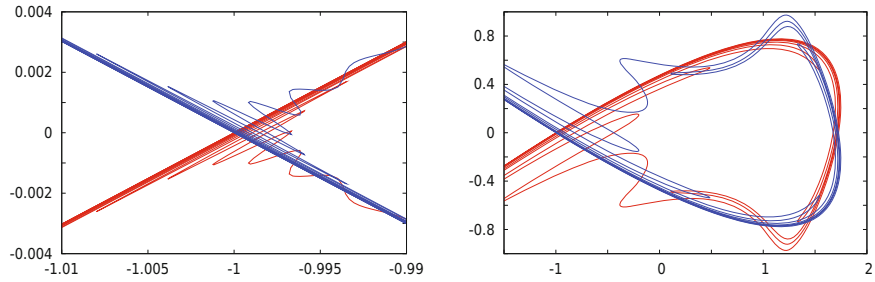

Figure 3.5: *Left:* a magnification of Figure 3.2 showing that the manifolds do not coincide. *Right:* part of the invariant manifolds of the hyperbolic point H for $c = 0.77$ (the unstable manifold in red, the stable one in blue). One has $W_H^s = S(W_H^u)$. The splitting of the manifolds is now clearly visible. It is increasing with c. Note that the domain around the point E which is not covered by the oscillations of the manifolds, becomes smaller. Compare with the non escaping set of points in Figure 3.2 right, for a nearby value of c.

A measure of the lack of coincidence of W^u and W^s is the *splitting angle*. This is defined as the angle between manifolds at a given homoclinic point. In the present case of quadratic APM, we can measure the angle at the first intersection of the manifolds with $y = 0$ to the right of $x = 1$ and see how it behaves as a function of c. For concreteness, we denote this angle as $\sigma(c)$. In Figure 3.6, left and middle, we represent the value of $\sigma(c)$ in different scales. In the left-hand plot, despite the splitting being different from zero for any $c > 0$, we see that only for $c > 0.2$ does it start to be visible. To make visible what happens for small c, we display, in the middle plot, $\log(\sigma)$ against $\log(c)$. Note that already for $c = 0.05$ the value of $\sigma(c)$ is below 10^{-15} and, hence, it is negligible for any practical application.

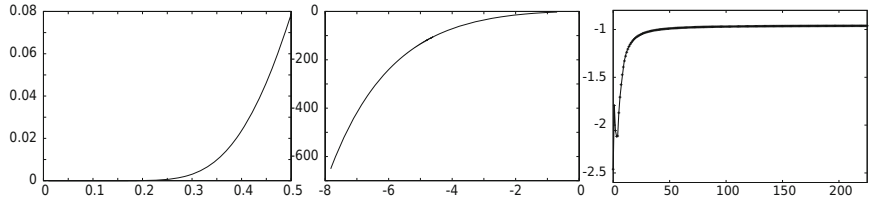

Figure 3.6: Different representations of the splitting angle $\sigma(c)$ between the manifolds at the first intersection with $y = 0$, $x > 1$. *Left:* σ, as a function of c, showing that σ seems negligible for $c < 0.2$. At that value of c, the first digits are $\sigma(c) = 6.21463426856826630097675406749853074250 03 \ldots \times 10^{-5}$. *Middle:* $\log(\sigma)$ as a function of $\log(c)$, which allows to see how small $\sigma(c)$ is for c approaching zero. *Right:* the values of $\log_{10}(\omega_{2m}(2\pi^2)^{2m}/(2m+6)!)$ versus m, to give evidence of the Gevrey character of $\Omega(h)$ (see text).

Concerning the right-hand plot in Figure 3.6 we need some preliminaries. Let $\lambda(c)$ be the *dominant eigenvalue* at the point H, which is equal to $1+c+\sqrt{2c+c^2}$ for F_c. An essential parameter in the theoretical study of the problem is $h(c) = \log(\lambda(c))$, because using suitable representations of the manifolds, it is possible to show that the splitting has upper bounds of the form $\exp(-\eta/h)$, where η is related to the *imaginary part of the singularity of the separatrix of the limit flow*, as mentioned before in Figure 3.2. This type of result is true for general analytic APM close to the identity map, see [10, 11]. In fact, for the present problem one can prove a more precise result. The splitting angle has the form

$$\sigma(c) = \frac{9}{2} \times 10^6 \pi^2 h(c)^{-8} \exp\left(-\frac{2\pi^2}{h(c)}\right) \times \Omega(h). \tag{3.9}$$

The term $\Omega(h)$ can be expanded in powers of h^2, say $\Omega(h) = \sum_{m\geq 0} \omega_{2m} h^{2m}$, and can be bounded by $\omega_0 + \mathcal{O}(h)$. The constant term can be determined numerically and the first digits of ω_0 are 2.48931280293671. Note, however, that the series defining $\Omega(h)$ is divergent. But for every value of h it provides a good approxima-

tion if we truncate the summation at the appropriate place. There is numerical evidence that the series is of *Gevrey-1 class*.

A formal power series $\sum c_k t^k$ is said to be of Gevrey-β class if the series $\sum c_k (k!)^{-\beta} t^k$ is convergent. We can compute the series $\sum_{m\geq 0} \omega_m h^{2m}/(2m)!$ obtained from $\Omega(h)$ using $\beta = 1$. From a numerical determination of $\Omega(h)$, for different values of h, one can obtain the coefficients ω_{2m}. See [12] for methodology and examples. In the right-hand plot in Figure 3.6 we display $\log_{10}(\omega_{2m}(2\pi^2)^{2m}/(2m+6)!)$ as a function of m, which seems to tend to a constant. This gives evidence of the Gevrey-1 character of $\Omega(h)$ we mentioned. But to prove this fact is an open problem.

See slides (H) for the role of the splitting phenomena in the measure of the chaotic domain in different problems.

On the destruction of invariant curves

As mentioned in the part about invariant submanifolds in Section 3.2.1, if ρ is too close to a rational (in the Diophantine sense), or if the twist condition is too weak, or if the perturbation ε with respect to an integrable map is too large, the IC does not exist. These analytic properties also have a nice geometric interpretation.

To illustrate the mechanism leading to the destruction of ICs we consider Figure 3.7. It has been produced for $c = 0.618$ (left) and $c = 0.63$ (right) and it only shows the left-hand part of the set of points which have bounded orbits. The case of Figure 3.7 is similar to the one on the Figure 3.2 right, but now the main islands are 6-periodic instead of 5-periodic.

On the left-hand plot one can see medium size islands with $\rho = 3/19$ (one of them with its central elliptic point on $y = 0$) and two symmetrical islands, in the same family, with $\rho = 4/25$, as well as several satellite islands, then tiny islands (e.g., with $\rho = 17/107, 39/245, 11/69, 19/119, 21/131, 13/81, \ldots$) and ICs. In particular, some ICs are still present between the two chains of medium size islands. Some other ICs, surrounding the main period-6 islands (not displayed), appear as the rightmost curves shown.

On the right-hand plot we display in black two chains of islands of rotation numbers $3/19$ and $4/25$, corresponding to the ones in the left plot, but now they are smaller. Consider the associated hyperbolic periodic orbits, the one with rotation number $4/25$ being visible on the x-axis and the two symmetric points belonging to the hyperbolic periodic orbit of rotation number $3/19$ being close to $x = -0.2$ off the x-axis. The manifolds of these periodic orbits give rise to *heteroclinic connections*, that is, intersections of the stable and unstable manifolds of two different objects. The manifolds $W^u_{4/25}, W^s_{4/25}$ are shown in red and green, respectively. The manifolds $W^u_{3/19}, W^s_{3/19}$ are shown in blue and magenta, respectively. Note that $W^u_{4/25}$ and $W^s_{3/19}$ (and, symmetrically, $W^s_{4/25}$ and $W^u_{3/19}$) have *transversal* heteroclinic intersections. This produces an obstruction to the existence of the ICs which could separate the chains of islands. This is the basis of the so-called *obstruction mechanism* [38].

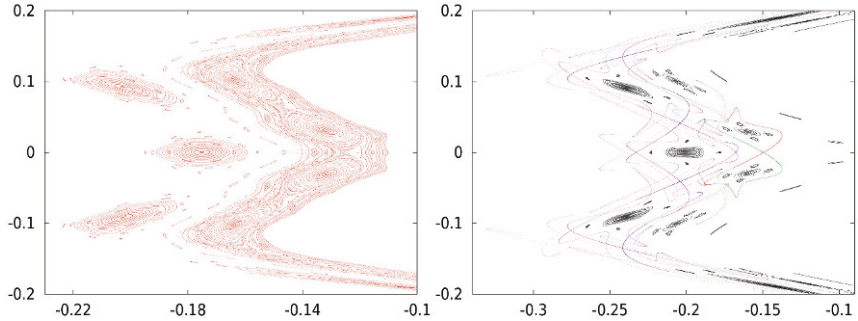

Figure 3.7: *Left:* A part of the set of non escaping points for the map F_c and $c = 0.618$. *Right:* similar plot for $c = 0.63$, displaying also several invariant manifolds of periodic hyperbolic points leading to heteroclinic intersections. See the text for details.

Indeed, if we consider a curve formed by a piece of invariant manifold of the inner hyperbolic periodic point (the one of period 25) until the heteroclinic point, followed by a piece of invariant manifold of the outer hyperbolic periodic point (the one of period 19), from the heteroclinic point to the periodic one, the ICs will have to cross it. This is impossible because of the invariance. In fact, one concludes that ICs with $\rho \in (3/19, 4/25)$ cannot exist. But ICs with ρ in that interval are found for $c = 0.618$. Hence, the geometrical mechanism responsible for the destruction is the existence of heteroclinic connections which obstruct the possible curves.

Anyway, there are invariant objects with ρ in the above mentioned interval. It is proved that they should be at the outer part of the manifolds of the hyperbolic periodic orbit with $\rho = 4/25$ and at the inner part of the manifolds of the hyperbolic periodic orbit with $\rho = 3/19$. The heteroclinic intersections of these manifolds create *gaps* which forbid the existence of points of the invariant object in them. As a consequence, the invariant object which remains for some irrational $\rho \in (3/19, 4/25)$ is a *Cantor set* [29, 30]. Points which were located inside an IC for $c = 0.618$ and, hence, without possible escape, can now, for $c = 0.63$, find a gap of the Cantor set and escape under iteration. It looks like some random process and, certainly, the probabilities are related to the size of the gaps in the Cantor set.

3.2.2 The standard map

Looking at the right-hand plot in Figure 3.2 we clearly see the period-5 islands around period-5 elliptic points and, as already said, we can guess the existence of period-5 hyperbolic points. We also see ICs close to the island, some of them inside, which have $\rho > 1/5$, and others outside, which have $\rho < 1/5$. If instead of iterations under F_c we iterate using F_c^5 we will check that the inside curves turn

a little clockwise and the outside ones turn a little counterclockwise. We can ask: what happens for an APM if we have two ICs turning by iteration a small amount in opposite directions?

This is the contents of the so-called *last geometric theorem by Poincaré*. Between the two curves, invariant under a map M, there should appear fixed points, generically isolated and alternatively elliptic and hyperbolic. Typically, one point of each type appears. But if the map is the q-th power of some other map $\tilde{M}$, with rotation number p/q, $(p,q)=1$, then there are q fixed points of each type under M, which are q-periodic under $\tilde{M}$.

The structure of the islands is reminiscent of the phase portrait of a pendulum, whose Hamiltonian is $H(x,y)=y^2/2+\cos(x)$ using suitable coordinates. From a quantitative point of view (the width of the islands) we recall that the maximal distance between upper and lower separatrices in a pendulum with Hamiltonian $H(x,y)=y^2/2+\delta\cos(x)$ is $4\sqrt{\delta}$. But we keep the presentation in the scaled version, i.e., with the coefficient of the cosine equal to 1. The equations are $\dot{x}=y$, $\dot{y}=\sin(x)$. One can think of a discrete model which, in the limit, behaves as the pendulum. The simplest approach would be to use an explicit Euler method with step h, which gives the map $(x,y)\to(x+hy, y+h\sin(x))$. Unfortunately, that map is not an APM, but can be made symplectic using a symplectic Euler method: $(x,y)\to(\bar{x},\bar{y})$, $\bar{y}=y+h\sin(x)$, $\bar{x}=x+h\bar{y}$. If we do not like to have the parameter h in both variables, we simply replace hy by a new variable z, rename z again as y, introduce $k=h^2$, and we obtain

$$SM_k:\begin{pmatrix} x\\ y\end{pmatrix}\to\begin{pmatrix} \bar{x}=x+\bar{y}\\ \bar{y}=y+k\sin(x)\end{pmatrix}, \tag{3.10}$$

a popular map known as a *standard map* [7]. It is clear that we can look at the variables (x,y) in $\mathbb{S}\times\mathbb{R}$ or in $\mathbb{T}^2$. It has fixed points located at $(0,0)$, hyperbolic, and at $(\pi,0)$, elliptic, that we denote again as H and E. Figure 3.8 displays the phase portrait (in $\mathbb{T}^2$) for $k=0.5$ and $k=1$.

On the left-hand plot it is hard to see that the stable and unstable manifolds of H do not coincide. A study like the one in the invariant manifolds part of Section 3.2.1 reveals similar properties. But the strongest difference between these plots is that in the left one there exist rotational ICs, that is, ICs going from the left vertical boundary to the right one (in this representation; in fact these boundaries are identified). These curves are absent in the right plot. Hence, if we consider the map in $\mathbb{S}\times\mathbb{R}$, there is no obstruction to the dynamics in the y direction for $k=1$. There are points with an initial value $y\in[0,2\pi)$ whose iterates can go arbitrarily far away in the y direction (despite the fact that for that value $k=1$ will require many iterates).

The critical value up to which one has rotational ICs is the so-called *Greene's critical value* $k_G\approx 0.971635$; see [19]. The "last" rotational IC which is destroyed has $\rho=(\sqrt{5}-1)/2$, the golden mean. This is not a surprise; it is the number in $(0,1)$ with best Diophantine properties. The obstruction method using hyperbolic

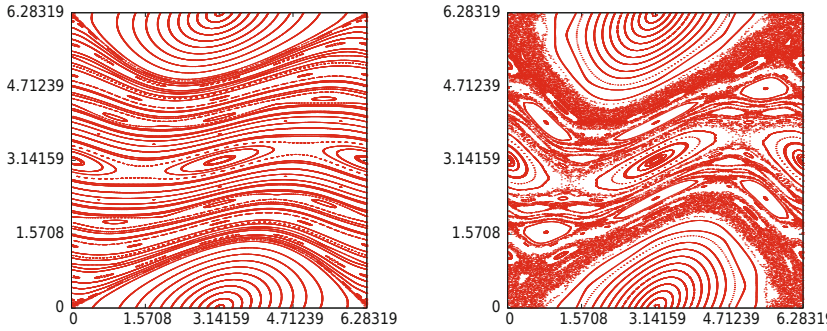

Figure 3.8: Phase portrait of (3.10). *Left:* for $k = 0.5$, still quite well ordered. *Right:* for $k = 1$, already with a big amount of chaos. Beyond the main elliptic island around E one can see several islands in both cases. The largest chaotic zone appears around the invariant manifolds of H.

periodic orbits with rotation numbers of the form F_{n-1}/F_n and F_n/F_{n+1}, F_n being the n-th Fibonacci number, plus a suitable extrapolation, allows us to determine k_G accurately. Note also that for $k > k_G$ but close to k_G, the rotational IC with $\rho = (\sqrt{5}-1)/2$ is replaced by a Cantor set with "small holes". This supports the claim about the large number of iterates needed to have y far away from the initial location. *Renormalization theory* [26, 27] provides the framework to understand those things in detail. For large values of k the standard map has interesting *statistical properties*. But they can be strongly affected by the role of the islands, see [32].

On the other hand, the Hamiltonian $H(x, y) = y^2/2 + \cos(x)$ can be replaced by more complex ones to obtain generalized standard maps. Adding terms in y^3 and $y\cos(x)$ allows us to explain the asymmetry which can be seen in Figure 3.2, right between the inner part and the outer part of the islands and the related inner, and outer splittings of the manifolds of the associated periodic hyperbolic points [52], in contrast with the symmetries of a pendulum. Replacing $y^2/2$ by $-by + y^3/3$ allows us to reproduce a limit flow of the meandering curves, as shown in Figure 3.4, and other more complicated changes give rise to labyrinthine ICs with funny shapes [43].

3.2.3 Return maps: the separatrix map

A useful device to understand the dynamics when some hyperbolic invariant object $\mathcal{A}$ has orbits homoclinic to it are the *return maps*. Assume that we have an initial point in a given domain $\mathcal{D}$ close to a point homoclinic to $\mathcal{A}$. Then it approaches $\mathcal{A}$ under iteration, close to $W^s_{\mathcal{A}}$, and after the passage near $\mathcal{A}$ moves away, close to $W^u_{\mathcal{A}}$, and returns to $\mathcal{D}$. Can we describe how the return is produced?

To illustrate with an example we have used a modified Hénon–Heiles potential. In a pioneer example Hénon and Heiles in 1964 used a Hamiltonian with two d.o.f. (a model of the motion of a star in a galaxy with cylindrical symmetry) [21]. The Hamiltonian they derived is

$$HH(x, y, p_x, p_y) = (x^2 + y^2 + p_x^2 + p_y^2)/2 + x^3/3 - xy^2, \tag{3.11}$$

and a careful study of the behaviour of nearby orbits of the system (3.11) lead to the detection of chaotic motion, giving evidence of the lack of integrability, a fact that was proved theoretically later and that was relevant to face integrability problems from an algebraic point of view; see [34] and references therein. Later on the family with Hamiltonian $HH_c(x, y, p_x, p_y) = (x^2 + y^2 + p_x^2 + p_y^2)/2 + cx^3 - xy^2$ was introduced, and the case $c = 0$,

$$HH_{c=0}(x, y, p_x, p_y) = (x^2 + y^2 + p_x^2 + p_y^2)/2 - xy^2, \tag{3.12}$$

that we shall use as illustration, presents some interesting particularities. Like many other simple models it has a symmetry with respect to simultaneous change of sign of y and t.

One can fix the value of the energy and use $y = 0$ as a Poincaré section. The Poincaré map $\mathcal{P}$ has a fixed point H which corresponds to a hyperbolic periodic orbit of (3.12). The invariant manifolds on $HH_{c=0}^{-1}(0.115)$ are shown in Figure 3.9. There exist homoclinic points and the symmetry implies that the upper branch of W_H^s can be obtained from the lower branch of W_H^u.

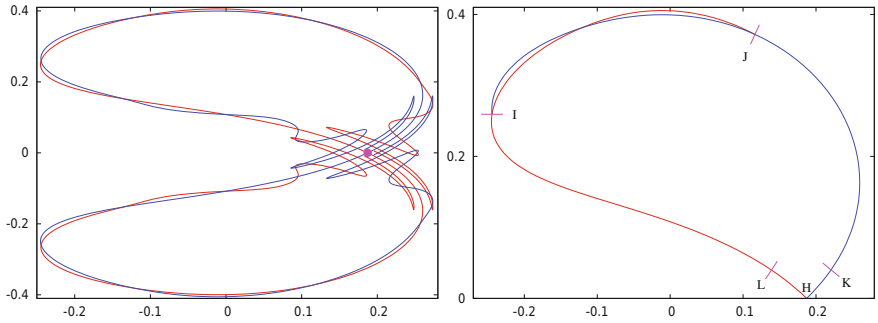

Figure 3.9: *Left:* the invariant manifolds (W^u in red, and W^s in blue) of the hyperbolic simple periodic orbit of the modified Hénon–Heiles Hamiltonian located inside the domain of admissible conditions on the Poincaré section $y = 0$, for the level of energy $h = 0.115$. The variables displayed are (x, p_x). *Right:* a magnification of the upper part showing the location of sections I, J, K, and L mentioned in the text. The periodic orbit appears marked as H on the section.

Our goal is to describe the return to a suitable domain $\mathcal{D}$ as a model for a general setting. In Figure 3.9 on the right there is a homoclinic point in the segment

market as I, whose image under $\mathcal{P}$ is the segment marked as J. A suitable domain can be a strip around the parts of the manifolds between I and J. Note that in the present case, due to the symmetry, we consider in Figure 3.9 (right) only the upper part in the (x, p_x) variables. It can happen that, after passage near H, a point moves to the lower part. Hence, it is convenient to consider $\mathcal{D}$ as the union of two strips, symmetric the one with the other, and that we can denote as $\mathcal{D}_+$ and $\mathcal{D}_-$, according to the sign of p_x, and define $\mathcal{D} = \mathcal{D}_+ \cup \mathcal{D}_-$.

In general, there is no symmetry and then $\mathcal{D}_-$ is not obtained from $\mathcal{D}_+$ by symmetry, and even some of the branches of the manifolds can escape, as it happens for (3.5).

If we take the part of W^u_H from H to the homoclinic point which appears in J, followed by the part of W^s_H between the homoclinic and H, and add the symmetric part (on $p_x < 0$) we have a *figure-eight pattern* which appears in many problems. This occurs, e.g., in the manifolds of the hyperbolic fixed point of (3.10). Looking at the map in $\mathbb{S} \times \mathbb{R}$ in suitable coordinates, one has also a figure-eight pattern [53].

First we assume that a point is located in $\mathcal{D}_+$ below W^s_H (the line in blue). After passing close to H it will return to $\mathcal{D}_+$. We follow an elementary method to find the return map. If the splitting is small enough we can assume that the upper branches of the manifolds are coincident and consider a nearby integrable map in the domain bounded by the branches of the manifolds. Let φ_t be the flow of a Hamiltonian v.f. with one d.o.f. in (x, p_x) with Hamiltonian $\mathcal{H}$ such that $\varphi_{2\pi}$ coincides with this integrable map. In particular, points in I move to points in J under $\varphi_{2\pi}$, and we can redefine the strip $\mathcal{D}_+$ as the set $\cup_{t\in[0,2\pi]}\varphi_t(I)$. The manifolds $W^{s,u}_H$ under that Hamiltonian v.f. coincide and form the separatrix of $\mathcal{H}$. As additional variable in $\mathcal{D}_+$, transversal to that separatrix, we take the level h of $\mathcal{H}$, assuming $\mathcal{H}$ is positive inside the separatrix and equal to zero on it.

For concreteness, let us denote as λ the dominant eigenvalue of the differential of the map $\varphi_{t=1}$ at H. It is clear that the dominant eigenvalue for $\varphi_{t=2\pi}$, close to the one of the initial map, say μ, is $\lambda^{2\pi}$ and that for the Hamiltonian v.f. is $\log(\lambda)$. If λ is close to 1 then $\log(\lambda)$ will be close to zero. For simplicity, we denote $\log(\lambda)$ as λ^*. In terms of the dominant eigenvalue of the initial map one has $\lambda^* \approx \log(\mu)/(2\pi)$.

As all the orbits in the domain bounded by the separatrix are periodic under the flow, when a point in $\mathcal{D}_+$ returns to it, it has the same value of h. But t has changed by the period, which behaves like $c - \log(h)/\lambda^*$, where c is a constant (essentially equal to the time to go from section L to section K). The map would be $(t, h) \mapsto (t + c - \log(h)/\lambda^* \,(\mathrm{mod}\, 2\pi), h)$.

Now we return to our original map. The only change is due to the lack of coincidence of W^s_H and W^u_H. If we consider the variable h defined as an energy with respect to W^u_H, when continuing the motion close to W^s_H the energy should be considered with respect to that manifold. There is a jump in energy due to the splitting. Note that, using a normal form around H, it is possible to define in a natural way an energy in a neighbourhood of this point, and to transport that

function along both manifolds, by backward or forward iteration, see [11], and also [50] in a general context. The two energies do not coincide in $\mathcal{D}_+$. The difference is the jump just mentioned. Let us denote it as $s(t)$ (it has a weak dependence on h that we neglect). The simplest expression for $s(t)$ is a sinusoidal oscillation $\varepsilon \sin(t)$ which measures the location of W^u_H with respect to W^s_H. Then the return map becomes

$$\begin{pmatrix} t \\ h \end{pmatrix} \to \begin{pmatrix} \bar{t} = t + c - \log(\bar{h})/\lambda^* \,(\mathrm{mod}\ 2\pi) \\ \bar{h} = h + \varepsilon \sin(t) \end{pmatrix}. \tag{3.13}$$

It is clear that the map is not defined if $\bar{h} = 0$ because then the point is in W^s_H. On the other, hand we have not considered the case $h < 0$. Then the process is similar, but we land on the lower domain $\mathcal{D}_-$. Beyond the variables (t, h) one has to consider a sign σ equal to ± 1 in $\mathcal{D}_\pm$. Using also the sign and renaming the variables as ξ, η, with $\xi \in [0, 2\pi)$ and η small, the map (3.13) becomes

$$SepM\colon \begin{pmatrix} \xi \\ \eta \\ \sigma \end{pmatrix} \to \begin{pmatrix} \bar{\xi} = \xi + c - \log(|\bar{\eta}|)/\lambda^* \,(\mathrm{mod}\ 2\pi) \\ \bar{\eta} = \eta + \varepsilon \sin(\xi) \\ \bar{\sigma} = \sigma \times \mathrm{sign}(\bar{\eta}) \end{pmatrix}, \tag{3.14}$$

a map known as a *separatrix map*. In a general case the jump $\varepsilon \sin(\xi)$ is replaced by a function $s(\xi)$. In the asymmetric cases one uses different jump functions $s_\pm(\xi)$ according to σ. The parameter ε, related to the size of the jump or splitting has, typically, exponentially small upper bounds as a function of some physical parameter, like the energy in the case of system (3.12). But in other cases, if the dominant eigenvalue at H tends to a constant $\lambda_0 > 1$ when some parameter γ tends to zero, it can be, simply, a power of γ.

For simplicity, we concentrate on the symmetric case and to points passing only through $\mathcal{D}_+$. Then $\sigma = 1$ and we discard it in (3.14). Now we assume that η is close to some fixed value, η_0, write $\eta = \eta_0 + \zeta$ and $\log(\bar{\eta}) = \log(\eta_0) + \log(1 + \bar{\zeta}/\eta_0) \approx \log(\eta_0) + \bar{\zeta}/\eta_0$, keeping only linear terms in $\bar{\zeta}$. This is a good approximation if $\bar{\zeta}/\eta_0$ is small. If we assume, also, that λ is close to 1, then λ^* is small. In the (ξ, ζ) variables the map becomes $(\xi, \zeta) \mapsto (\bar{\xi} = \xi + c_1 + b_1\bar{\zeta},\ \zeta + \varepsilon \sin(\xi))$, where $c_1 = c - \log(\eta_0)/\lambda^*$, $b_1 = -1/(\eta_0 \times \lambda^*)$, and we do not write explicitly that ξ is taken mod 2π. Finally, define new variables $u = \xi, v = c_1 + b_1\zeta$ and the map becomes

$$\begin{pmatrix} u \\ v \end{pmatrix} \to \begin{pmatrix} \bar{u} = u + \bar{v} \\ \bar{v} = v + b_1 \varepsilon \sin(u) \end{pmatrix}. \tag{3.15}$$

Comparing (3.15) with (3.10) we see that they are identical if we set $k = b_1\varepsilon = -\varepsilon/(\eta_0 \times \lambda^*)$. Therefore, we can expect to find invariant curves in the separatrix map at a distance $\eta_0 > \varepsilon/(k_G \times \lambda^*)$ from the location of the invariant manifolds in $\mathcal{D}_+$. A similar reasoning applies in the outer part, when the invariant curves make the full turn around the figure eight. This gives also an estimate of the width of

the zone with chaotic dynamics around the split manifolds. The estimate is quite realistic if ε is very small and λ is close to 1. This occurs, for instance, in a case like the Hamiltonian (3.12) because then, on a level of energy h, λ^* and ε are, respectively, of the order of h and exponentially small in h. See [47] for a study of several cases, with different number of d.o.f., either resonant or not.

As final comments in this subsection one has to add that it is very important to derive return maps in higher dimensions, like Hamiltonian systems with ≥ 3 d.o.f. or symplectic maps in dimension ≥ 4. But the formulas that one obtains can be far from simple, due to quasiperiodicity and resonances. To derive, from these return maps, bounds on the distance at which one can find invariant tori, speed of diffusion, etc, is an open problem. See slides (J) for other open problems associated to some classes of global bifurcations.

3.3 Some theoretical results, their implementation and practical tools

In this section we recall some general results and also provide tools to make them explicit.

3.3.1 A preliminary tool: the integration of the ODE, Taylor method and jet transport

In the case of an analytic Hamiltonian (or general) v.f. like $\dot{x} = f(t, x)$, $x(t_0) = x_0$, $(t_0, x_0) \in \Omega \subset \mathbb{R} \times \mathbb{R}^n$ or $\Omega \subset \mathbb{C} \times \mathbb{C}^n$, one should use integration methods of the initial value problem for ODE. For instance, having in mind to compute Poincaré iterates.

A quite convenient method is the *Taylor method*. That is, to obtain the Taylor expansion $x(t_0 + h)$ for suitable values of h. If $x(t_0 + h)$ has components x_i, $i = 1, \ldots, n$, we look for a representation

$$x_i = \sum_{s=0}^{N} a_i^{(s)} h^s, \tag{3.16}$$

for suitable N, h, and use it as a one-step method. For further reference we denote as $a^{(s)}$ the vector with components $a_i^{(s)}$.

The point is how to compute the coefficients of the expansion in an easy way to high order. For a very large class of functions the evaluation of f can be split

into simple expressions

$$\begin{aligned} e_1 &= g_1(t,x), \\ e_2 &= g_2(t,x,e_1), \\ &\vdots \\ e_j &= g_j(t,x,e_1,\ldots,e_{j-1}), \\ &\vdots \\ e_m &= g_m(t,x,e_1,\ldots,e_{m-1}), \\ f_1(t,x) &= e_{k_1}, \\ &\vdots \\ f_n(t,x) &= e_{k_n}. \end{aligned}$$

Each one of the expressions e_j contains a sum of arguments, a product or quotient of two arguments or an elementary function (like sin, cos, log, exp, $\sqrt{\ },\ldots$) of a single argument. The basic idea is to compute in a recurrent way the power series expansion (up to the required order) of all the e_j. The g_j have to be seen as operations with (truncated) power series. Hence, we can proceed as follows:

(i) Input: t and the components of x_0, that is, the coefficients of order zero in (3.16).

(ii) Step s, $s \geq 0$: from the arguments of g_j up to order s we obtain the order s terms of e_j; in particular for $f_j(t,x)$, which gives the order $s+1$ for x_j (dividing by $s+1$). This is repeated up to the required value of N.

(iii) The values of N, h can be selected so that the truncation error $\sum_{s>N} a_i^{(s)} h^s$ is bounded, for every component, by some small ε negligible in front of the (unavoidable) round off error.

Under reasonable assumptions, like $c_1\gamma^s \leq ||a^{(s)}|| \leq c_2\gamma^s$, $0 < c_1 < c_2$, (which implies radius of convergence $\rho = 1/\gamma$) in the limit when $\varepsilon \to 0$, say $\varepsilon = 10^{-d}$, with d large, one can take h such that the last term satisfies $||a^{(N)}||h^N = \varepsilon$. It turns out, concerning efficiency, that the optimal value of h tends to $\rho \times \exp(-2)$ (independently of the equation, and where ρ refers to the radius of convergence around the current point x_0), and $N \approx d\log(10)/2$ when $\varepsilon \to 0$.

To carry out step (ii) above is immediate for arithmetic operations. As an example for elementary functions we consider the case of powers, that we should use to integrate (3.1). Let $u(t) = \sum_{s\geq 0} u_s t^s$, $u_0 \neq 0$, $\alpha \in \mathbb{R}$, and we want to compute $v(t) = u(t)^\alpha = \sum_{s\geq 0} v_s t^s$. Then,

$$v_0 = u_0^\alpha, \quad v_s = -\frac{1}{su_0}\sum_{k=0}^{s-1} v_k u_{s-k}[k - \alpha(s-k)],$$

for $s > 0$, the determination being fixed by the one used for v_0. This follows easily from $v(t) = u(t)^\alpha$ by taking logarithms and differentiation with respect to

t. Similar recurrences can be obtained for any elementary function. If f contains special functions (e.g., Bessel functions) it is enough to add the ODE satisfied by these functions to the system to be integrated.

Computing to order N has a cost $\mathcal{O}(N^2)$. This is true for the most expensive elementary operations and functions, and it is the basis of the optimal estimates given above, see [22] and slides (A).

In the autonomous case, to obtain the image of a point for a Poincaré map $\mathcal{P}$ through a section Σ given by $g(x) = 0$ when g changes from < 0 to > 0, assume that we have a time t^* such that $g(\varphi_{t^*}(x_0)) < 0$ and $g(\varphi_{t^*+h}(x_0)) > 0$, for the current value of h. Finding $\mathcal{P}(x_0)$ reduces to solving a 1-dimensional equation, $g(\varphi_{t^*+\delta}(x_0)) = 0$, for the variable δ. This is easily done by using Newton's method.

Assume now that we look for a periodic solution. It can be written as a fixed point of a Poincaré map: $G(x_0) = \mathcal{P}(x_0) - x_0 = 0$, for $x_0 \in \Sigma$. Again this can be solved by Newton's method, but this requires that one knows the differential map $D\mathcal{P}(x_0)$. To this end we integrate, together with the v.f. f, the first order variational equations $\dot{A} = Df(\varphi_t(x_0))A$, $A(0) = \mathrm{Id}$. There are two points to take into account, see [40]:

(i) The admissible variations of x_0 should be confined to the tangent space to Σ at that point. Furthermore, if the system has first integrals, like in the Hamiltonian case, this gives additional constraints for x_0 and the admissible variations if we fix the levels of these integrals.

(ii) The return time to Σ depends on the initial point. If instead of leaving from x_0 we leave from $x_0 + \xi$, ξ being an arbitrarily small admissible variation, the landing time in Σ has to be corrected by terms $\mathcal{O}(||\xi||)$. This is relevant to computing $D\mathcal{P}(x_0)$.

In some cases (see Subsection 3.3.4) we can be interested in having an approximation of the Poincaré map not restricted to first order terms in the variations of $x_0 \in \Sigma$, but to higher order: we would like to have the Taylor expansion of $\mathcal{P}(x_0+\xi)$ to some given order in ξ. To this end, one can integrate the higher order variational equations, restrict the domain of definition to Σ and to the levels of the current first integrals, or proceed in a different, easier, way, using *jet transport*, described along the following lines.

This can be also applied to obtain the image of a neighbourhood of a point x_0 under φ_t, to see how it depends on parameters (useful to analyze bifurcations), etc.

Assume the initial conditions are $x_0+\xi$, where ξ are some variations and we want to obtain $\varphi_t(x_0+\xi)$ at order m in ξ. It is enough to replace all the operations described above to compute e_j, in order to obtain the coefficients in (3.16), done with numbers, by operations with polynomials in ξ up to order m. This applies to arithmetic operations, elementary functions, special functions, etc. Hence, instead of the vectors a^s of numerical coefficients in (3.16) we deal with tables containing the numerical coefficients, up to order m, of n polynomials in the ξ variables.

If we return to the case of the Poincaré map, we had to solve $g(\varphi_{t^*+\delta}(x_0)) = 0$, for the variable δ. Now δ will depend on ξ, but this is not a problem for Newton's method. We simply apply it by replacing numbers by polynomials in ξ.

We remark that the jet transport can be implemented in an efficient way. It is also possible to produce rigorous estimates of the tails at every step, and to obtain intervals which contain the correct values of all the coefficients. This allows us to convert a purely numerical simulation into a Computer Assisted Proof (CAP). See, e.g., [24].

3.3.2 Normal forms

To study many systems, a useful trick is to try to reduce them to an expression as simple as possible, according to the topics of interest. If we study a discrete map around a fixed point, it would be nice to be able to reduce it to a linear map. In general, this is not possible. Furthermore, we can be interested also in the dependence with respect to parameters, to analyze possible bifurcations.

For concreteness we face a Hamiltonian in n d.o.f., in Cartesian coordinates, around a fixed point (located at the origin) that we assume totally elliptic: the eigenvalues are $\exp(\pm \mathrm{i}\omega_j)$, $j = 1, \ldots, n$. In canonically conjugate variables (x_i, y_i), $i = 1, \ldots, n$, we write it as $H = \sum_{k\geq 2} H_k$, where H_k denote the homogeneous terms of order k and $H_2 = \sum_{i=1}^{n} \omega_i (x_i^2 + y_i^2)/2$. In principle, we try to make a change of variables to cancel the terms H_k, $k > 2$. To keep the Hamiltonian character of the v.f. we shall use canonical transformations. These can be easily obtained as the flow of an auxiliary Hamiltonian, G, with respect to an auxiliary time s until, say, $s = 1$. If you do not want to use a "so big time $s = 1$" simply scale $(x, y) \to \varepsilon(u, v)$, divide the Hamiltonian by ε^2 obtaining $H_2(u, v) + \varepsilon H_3(u, v) + \varepsilon^2 H_4(u, v) + \cdots$, and then the final value of s will be ε. But this is equivalent to the previous approach. What makes the change close to the identity is the smallness of (x, y), not the fact of using $s = 1$.

As we want to cancel, first, the terms in H_3, we shall represent G also as a sum of homogeneous parts, starting at order 3, $G = \sum_{k\geq 3} G_k$.

To transform the function H under the change we write $dH/ds = \{H, G\}$, where

$$\{H, G\} = \sum_{i=1}^{n} \frac{\partial H}{\partial x_i}\frac{\partial G}{\partial y_i} - \frac{\partial H}{\partial y_i}\frac{\partial G}{\partial x_i}$$

denotes the Poisson bracket. Note that the bracket of homogeneous polynomials of degrees d_1 and d_2 has degree $d_1 + d_2 - 2$. Higher order derivatives are obtained by doing, successively, the Poisson bracket with G once and again. Trying to cancel (if it is possible to cancel) the terms H_k, $k \geq 3$, we determine the homogeneous parts G_k. But it turns out that to obtain these parts it is much simpler to use complex coordinates. We introduce

$$\begin{pmatrix} x_i \\ y_i \end{pmatrix} = \frac{1}{\sqrt{2}} \begin{pmatrix} 1 & \mathrm{i} \\ \mathrm{i} & 1 \end{pmatrix} \begin{pmatrix} q_i \\ p_i \end{pmatrix}, \quad i = 1, \ldots, n.$$

Then H_2 becomes $\sum_{j=1}^{n} \mathrm{i}\,\omega_j q_j p_j$. The transformed Hamiltonian is

$$\varphi_{s=1}^{G}(H) = H + \{H, G\} + \frac{1}{2!}\{\{H, G\}, G\} + \frac{1}{3!}\{\{\{H, G\}, G\}, G\} + \cdots \quad (3.17)$$

Assume we have determined G_j, $j < m$, and we want to cancel all the possible terms to order m in (3.17). There are terms or order m in (3.17) which come from H_m or involving G_j, $j < m$, which are already known and that we denote, together, as K_m. For definiteness, assume $K_m = \sum_{a,b,|a|+|b|=m} K_{a,b}\, q^a p^b$, where a denotes a multiindex with n non-negative components a_i, $|a| = \sum_{i=1}^{n} a_i$, and $q^a = \Pi_{i=1}^{n} q_i^{a_i}$, as usual. Similarly for b and p^b. The only unknown part comes from G_m, that we also write as $G_m = \sum_{a,b,|a|+|b|=m} G_{a,b}\, q^a p^b$ and we would like to have

$$0 = \{H_2, G_m\} + K_m = \sum_{a,b,|a|+|b|=m} \mathrm{i}\,(\omega, b-a) G_{a,b}\, q^a p^b + \sum_{a,b,|a|+|b|=m} K_{a,b}\, q^a p^b, \quad (3.18)$$

where $(\omega,\, b-a)$ denotes the scalar product $\sum_{j=1}^{n} \omega_j (b_j - a_j)$. As $K_{a,b}$ is known, one easily determines $G_{a,b}$, provided $(\omega,\, b-a) \neq 0$. But it is clear that if $b_j = a_j$ for all j, then the term $K_{a,a}$ must be left on the transformed Hamiltonian, independently of ω. These are called the *unavoidable resonances* which appear at even orders. Furthermore, if ω is *resonant*, i.e., there are integers c_j, $j = 1, \ldots, n$, such that $(\omega,\, c) = 0$, other terms should be kept in the transformed Hamiltonian when $b - a = c$. These are the additional resonant terms.

The normalization process can be continued to any order. But, in general, unless the Hamiltonian is integrable, the formal normal form is not convergent. One can expect that it belongs to some Gevrey class (see the invariant manifolds part in Section 3.2.1), but I am not aware of *concrete general results* in that direction.

After we have transformed the Hamiltonian up to order M, we can skip the terms of higher order and denote the contribution up to order M as HNF_M, the *normal form to order* M. We recall that a Hamiltonian system with n d.o.f. is said to be *integrable* (in the Liouville–Arnold sense) if there exist n first integrals, F_j, $j = 1, \ldots, n$, an involution, $\{F_i, F_j\} = 0$, and functionally independent almost everywhere. If ω is non-resonant then the HNF_M is integrable, because one can take $F_j = q_j p_j$, $\forall j$.

Now consider the resonant case. By construction, $\{H_2, HNF_M\} = 0$ and, therefore, except in the degenerate case in which they are not independent, if $n = 2$ one has HNF_M integrable. In general this is not true if $n > 2$. The system can be far from integrable even in a small vicinity of a totally elliptic point. But it can take a long time to have numerical evidence of the existence of chaos, even if it occurs for most of the initial conditions.

A celebrated theorem by Arnold says that, for an integrable system, if the set of points in the phase space corresponding to fixed values of the first integrals $F_1^{-1}(c_1) \cup F_2^{-1}(c_2) \cup \cdots \cup F_n^{-1}(c_n)$ is compact, then it is an n-dimensional torus

$\mathbb{T}^n$. Around a given torus one can introduce the so-called *action-angle variables* (I, φ), $I \in \mathbb{R}^n$, $\varphi \in \mathbb{T}^n$. The integrable system can be written, then, as depending only on I: $H = H_0(I)$, the integration is elementary and the frequencies on the given torus have the expression $\omega_j = \partial H_0/\partial I_j|_{F=c}$, $j = 1, \ldots, n$. If the system is perturbed to $H = H_0(I) + \varepsilon H_1(I, \varphi)$ we can study how the properties of $H_0(I)$ change under the effect of the perturbation. See Subsections 3.3.3 and 3.3.5 in this direction.

But we want to point out that it is also possible to try to produce a normal form for the perturbed Hamiltonian around the given torus if the frequencies on it, ω_j, satisfy a non-resonant condition. This can push the perturbation to higher order in ε, making easier the applicability of general results.

Up to now we have considered, around a fixed point, the totally elliptic case. If the quadratic term H_2 contains some hyperbolic part $H_2 = \sum_{i=1}^{n_e} \omega_i(x_i^2+y_i^2)/2+ \sum_{j=n_e+1}^{n} \lambda_j x_j y_j$, one can use similar ideas to obtain approximations of the central manifold and of the Hamiltonian reduced to it. We return to this in Subsection 3.3.4.

3.3.3 Stability results: KAM theory and related topics

There is a natural generalization of the idea of twist map to higher dimension. Consider a map T defined, in suitable coordinates, in a product of n annuli, with radii $r_i \in (r_{d,i}, r_{u,i})$, $0 < r_{d,i} < r_{u,i}$, $i = 1, \ldots, n$, of the form $T(r, \alpha) = (r, \alpha + a(r))$, where $r \in \mathcal{R} = \Pi_{i=1}^n (r_{d,i}, r_{u,i})$ has components $r_1, \ldots, r_n$, $\alpha \in \mathbb{T}^n$ and a is a map from $\mathcal{R}$ to $\mathbb{R}^n$ which can be denoted as *translation*. The map T is an integrable symplectic map, and $\mathcal{R} \times \mathbb{T}^n$ is foliated by tori invariant under T. Nothing else but what we saw for (3.7) in the part about ICs in Section 3.2.1.

The differential of the translation with respect to the radii, $D_r a(r)$ is known as *torsion*.

Then the KAM theorem for symplectic maps has the following statement, completely analogous to Theorem 3.2.1.

Theorem 3.3.1. *Consider a perturbation $F_\varepsilon = T + \varepsilon P$ of the integrable symplectic map T in $\mathcal{R} \times \mathbb{T}^n$, and assume that for $r = r^*$ the vector $a(r^*)$ satisfies a DC, that the torsion is non-degenerate and ε is small enough. Then the map F_ε has also invariant tori in $\mathbb{T}^n$, close to $r = r^*$, and on them the action of F_ε is conjugated to the one of T on $r = r^*$, that is, a translation by $a(r^*)$.*

In the present case, the DC is slightly different from the one in (3.3). Beyond the translations $a_i(r)$, $i = 1, \ldots, n$, one has to add the value 1, as it is obvious thinking on the suspension. So, it reads as

$$\left| (\sum_{i=1}^{n} k_i, a_i) + k_0 \right| \geq b|k|^{-\tau}, \quad \forall k \in \mathbb{Z}^{n+1} \setminus \{0\},$$

where k denotes now $(k_1, \ldots, k_n, k_0)$. The role of the DC, the non-degeneracy of

the torsion, is analogous to the twist condition, and the smallness of ε plays the same role.

A result similar to Theorem 3.3.1 holds in the case of Hamiltonian systems.

Theorem 3.3.2. *Let $H_0(I)$ be an integrable Hamiltonian, for which there exist invariant tori, and assume that for some given torus, labelled by I^*, the frequencies $\omega(I^*) = \partial H_0(I)/\partial I|_{I=I^*}$ satisfy a DC (in the sense of* (3.3)*) and are non-degenerate, so that the differential $\partial\omega/\partial I|_{I=I^*}$ is regular. Then if ε is small enough, a perturbed Hamiltonian $H(I,\varphi) = H_0(I) + \varepsilon H_1(I,\varphi,\varepsilon)$ has a nearby invariant torus with the same frequencies.*

These results usually do not give estimates on how small ε should be or, if any, they are very pessimistic. However, normal form techniques (see Subsection 3.3.2) can help to start the iterative process in a very good approximation, so that the difference with the initial guess and the true torus, if it exists, is sufficiently small.

For the effective computation of invariant tori there exist different methods.

A quite classical method is the Lindstedt–Poincaré (LP) method. In principle, it is formal because one looks for the invariant tori without paying too much attention to the DC (despite the fact that this can also be implemented). Assume that we look for 2D tori around a totally elliptic point (assumed to be located at the origin) in a Hamiltonian system with $n = 2$ d.o.f. Let $\omega_1(0)$, $\omega_2(0)$, be the frequencies at the fixed point. The linear system will have, for the q, p variables, a representation as linear combinations of $\cos(\omega_1(0)t + \psi_1)$ and $\cos(\omega_2(0)t + \psi_2)$, where ψ_1, ψ_2 represent some phases, and these terms have amplitudes α_1, α_2. Due to symmetries and the freedom to select the origin of time, the phases for the different variables can be put in simple form.

We wish to satisfy the equations $\dot{q} = \partial H/\partial p$, $\dot{p} = -\partial H/\partial q$ by expanding in powers of the amplitudes α_1, α_2 and integration of the coefficients of these powers with respect to time. However, it turns out that at some order we can find on the right-hand side of the equations terms which are not purely quasiperiodic, i.e., they are constant. The solution consists in allowing the frequencies to depend also on the amplitudes. So $\omega_i = \omega_i(0) + \sum_{j_1,j_2} c_{i,j_1,j_2}\alpha_1^{j_1}\alpha_2^{j_2}$, $i = 1, 2$, and a suitable choice of these c_{i,j_1,j_2} coefficients cancels the constant terms.

An often used method is based in writing the coordinates of the points of the unknown torus as Fourier series in some angles, and then imposing the invariance conditions. For concreteness we consider the case of symplectic maps. The flow case can be reduced to this one via a Poincaré map. Assume that we look for a d-dimensional torus in which the dynamics is conjugated to $\theta \mapsto \theta + \alpha$, for $\theta \in \mathbb{T}^d$ and a translation vector $\alpha \in \mathbb{R}^d$ satisfying the DC. Let x be the coordinates in the phase space and F the discrete map. The invariance condition is

$$F(x(\theta)) = x(\theta + \alpha). \tag{3.19}$$

It is clear that one has freedom to select the origin of the angles θ_i and that eventual symmetries can reduce the number of coefficients to be determined.

To begin with the process, we can assume that we have obtained some approximation by direct numerical simulation, or that we start near a fixed (or periodic) point and use the linear approximation or an approximation obtained by an LP method. If we are interested in a family of invariant tori, one can use continuation methods, but taking into account that the values of α should satisfy the DC. Hence, there will be gaps in the family, despite the fact that they can be very small in some cases. Let c denote, generically, the coefficients of the Fourier expansion, truncated at a suitable order. From a grid of values of θ one can obtain initial values of x. They are mapped to $F(x)$ and the images can be Fourier analyzed to obtain the new Fourier coefficients $\hat{c}$. Let L be the action of the translation by α on the initial Fourier coefficients. According to (3.19), we should require $L(c) - \hat{c} = 0$. This is the equation that follows from (3.19) and has to be solved, usually by Newton's method. The differentials of the Fourier synthesis and analysis are elementary and the one of F can be obtained by computing DF (this can be, typically, the differential of a Poincaré map). See [23] for an efficient implementation with similar and extended ideas, which works even with a very large number of harmonics.

The number of harmonics to be used depends on the shape of the torus. One can use in the grid in θ (and, therefore, in x) a number of points larger than the number of components of c. In that way one can check the behaviour of coefficients in $\hat{c}$ which have not been used as c coefficients in the representation of the solution we search, and see if they can be neglected. Otherwise, one increases the number of harmonics. This can be done at successive iterations of Newton's method in a dynamic way.

It is also possible not to fix α a priori and determine it together with the coefficients c. Note that, in case α is close to resonant, one can have convergence problems. For other quite different problems, like looking for invariant tori in PDE, this method requires a huge number of Fourier coefficients if the discretisation dimension is large. Other methods, working directly in the phase space like the synthesis of a return map, see [39, 42], can give the desired results.

There is a fact, concerning invariant tori and which applies also to the computation of some periodic orbits, which can produce difficulties. This is the instability present in partially normally hyperbolic tori or, in a simpler case, in linearly unstable periodic orbits. Given a point x, and assuming it approximately located in an invariant torus, the instability can produce that $F(x)$ is far away from the torus. This produces convergence problems.

The solution consists in using *parallel shooting*. Instead of taking a single Poincaré section, say Σ, one can use several of them, say $\Sigma_0 = \Sigma, \Sigma_1, \Sigma_2, \ldots, \Sigma_{m-1}$, and the corresponding *partial Poincaré maps*:

$$\mathcal{P}_1 \colon \Sigma_0 \mapsto \Sigma_1, \quad \mathcal{P}_2 \colon \Sigma_1 \mapsto \Sigma_2, \quad \ldots \quad \mathcal{P}_m \colon \Sigma_{m-1} \mapsto \Sigma_0.$$

Hence, the full Poincaré map can be written as $\mathcal{P} = \mathcal{P}_m \circ \cdots \circ \mathcal{P}_2 \circ \mathcal{P}_1$. Then we look for Fourier representations in each one of the intermediate sections. This

produces a much larger set of equations, but it has the advantage that each one of the partial maps $\mathcal{P}_j$ is much less unstable.

In the case of highly unstable periodic orbits things are simpler. We only need one point in each intermediate section, say $x_0 \in \Sigma_0$, $x_1 \in \Sigma_1$, ..., $x_{m-1} \in \Sigma_{m-1}$. The conditions are simply $\mathcal{P}_1(x_0) - x_1 = 0$, $\mathcal{P}_2(x_1) - x_2 = 0$, ..., $\mathcal{P}_m(x_{m-1}) - x_0 = 0$. The system to be solved is large but the differential has a simple block structure and the condition number is much better.

3.3.4 Invariant manifolds

Another basic ingredient of the dynamics are the invariant manifolds. In contrast with the tori of maximal dimension, responsible for the regular behaviour, the invariant manifolds are, typically, responsible for the chaotic part of the dynamics. We comment first on invariant stable and unstable manifolds of fixed points of APM F. The components will be denoted as F_1, F_2.

Assume a fixed point is located at the origin with dominant eigenvalue $\lambda > 1$, and having an unstable linear subspace E^u and a stable one E^s. Then the *unstable manifold Theorem* ensures the existence of an unstable manifold $W^u_{\rm loc}$ in a neighborhood of the origin, invariant under F, tangent to E^u at the origin and such that for a point p on it, the iterates under F^{-1} tend to the origin. In fact, only the points in $W^u_{\rm loc}$ remain on the neighborhood for all iterations. This is a local result. Then the global unstable manifold W^u is obtained by iteration of $W^u_{\rm loc}$ under F. A similar result gives the stable manifold, obtained by exchanging F and F^{-1}. In the analytic case, as we assume, the manifolds are analytic.

Let u and s be local coordinates along the unstable and stable eigenvectors. For the linear map DF, the manifold W^u is just $s = 0$. We can try to find a representation of W^u for F as the *graph of a function*: $s = g(u) = \sum_{j\geq 2} a_j u^j$. The invariance condition reads $F_2(u, g(u)) = g(F_1(u, g(u)))$. The coefficients a_j are determined in a recurrent way by identifying the left-hand and right-hand coefficients of u^j.

An alternative representation of W^u is the *parametrization method*. Let us use z as a parameter. In the linear case, a point with $u = z$ is mapped to $u = \lambda z$. Now it is not necessary to use coordinates adapted to the eigenspaces. If we use (x, y) as coordinates around the fixed point and represent the parametrization as $(p_1(z), p_2(z))$, the invariance condition is simply

$$F(p_1(z), p_2(z)) = (p_1(\lambda z), p_2(\lambda z)). \tag{3.20}$$

That is, we look for a conjugacy on the manifold between F and its linear part. We search now for the parametrization as $p_1(z) = \sum_{j\geq 2} a_j z^j$, $p_2(z) = \sum_{j\geq 2} b_j z^j$ in (3.20). Note that the parametrization can be normalized so that the vector of coefficients of order 1 has Euclidean norm equal to 1. As before, the coefficients of order $j > 1$ are obtained in a recurrent way. This is the method used for many of the examples displayed before.

A first practical question, given a parametrization to order N (a similar question can be posed for the graph method), is up to which value of z, say $z_{\max}$, one can use the representation. The idea is quite simple: given a tolerance ε we can compute the point B of parameter z and also the point A of parameter z/λ. One should have $F(A) = B$, according to (3.20). Hence, we can check up to which value of z one has $||F(A) - B|| < \varepsilon$. This gives the admissible domain for z. Then, a *fundamental domain* $\mathcal{FD}$ is parametrized by $z \in (z_{\max}/\lambda, z_{\max}]$. Any point on the manifold can be found as an iterate of a point in $\mathcal{FD}$. A similar domain, with $z < 0$, has to be found for the other branch of the manifold.

To obtain points in the manifold for $z > z_{\max}$ we simply divide the current parameter by λ as many times as required until a value less than $z_{\max}$ is obtained. Assume one has to divide k times. Then we compute the point of parameter z/λ^k and iterate it k times under F. In this way it is possible to reach points away from the fixed one, to detect foldings of the manifold, to reach the vicinity of a homoclinic or heteroclinic point, etc. The selected values of z at which the computation is done can be chosen to satisfy conditions such as having the distance between two consecutive points in W^u or the angle between three consecutive points below some prefixed values.

Why do we need approximations beyond the linear one? The answer depends on the purpose. If we want to produce a long part of the manifold and, especially, if λ is close to 1, we can require many iterates. On the other hand, if F is not given explicitly but follows from a Poincaré map, we need jet transport to have a local Taylor expansion. In any case, there is an optimal choice to obtain the "cheaper order" (cheaper can mean in terms of CPU time, of personal time, or a combination of both).

If we are interested in locating a homoclinic point, and no symmetry is available for this, the problem reduces to finding two parameters, z_u and z_s, and well as two integers, k_u and k_s, to be used for the unstable and stable manifolds, respectively, such that $F^{k_u}(p_u(z_u)) = F^{-k_s}(p_s(z_s))$, where p_u, p_s denote the respective parametrizations. It is possible to find suitable values of k_u, k_s and then to solve for z_u, z_s using Newton's method. A similar method can be used for heteroclinic points, for tangencies, etc.

The ideas are similar in higher dimension. One can look for d-dimensional invariant manifolds, $d > 1$, using either graph or parametric methods. This is specially necessary, for instance, if we look for an unstable manifold with quite different eigenvalues. A low order representation will take the initial points along the direction of the maximal eigenvalue. Beyond using high order local expansions, to decrease the problem, one can use different devices depending on the problem.

To look for the invariant unstable manifold of an invariant curve in a symplectic 4D map, a parametrization using a parameter z, which measures the distance to the curve, and an angle θ along the curve are useful. The fundamental domain, in that case, is diffeomorphic to an annulus. See an example in Subsection 3.4.2 in a different context, and another one in Subsection 3.4.5 concerning a family of invariant curves.

The idea extends to any dimension with increasing complexity. See [2, 3, 4] for a nice global approach.

A different problem appears when we consider symplectic maps in dimension 4 (or higher) or problems reducible to them. Consider again the case of a fixed point but assume that, together with an eigenvalue $\lambda > 1$ and its inverse, there is a couple of eigenvalues of modulus 1. They give rise to the *centre manifold* of the point. In general, when we consider a given neighborhood of the point, the manifold has some degree of differentiability which depends on the neighborhood. Furthermore, there is no uniqueness in general.

The difficulty comes from the fact that the dynamics on that manifold is not known. It can contain, simultaneously, invariant curves, periodic points and chaotic zones. It is said to be a *normally hyperbolic invariant manifold* (NHIM) if the hyperbolicity normal to the manifold is stronger than the hyperbolicity that can be found inside the manifold.

One can recur to normal forms to obtain an approximation of all the dynamics around the point and, in particular, the centre manifold. A similar idea is to use a *partial normal form*, see [42]. Assume we have a Hamiltonian

$$H = \lambda q_1 p_1 + \frac{1}{2}\omega_1(q_2^2 + p_2^2) + \frac{1}{2}\omega_2(q_3^2 + p_3^2) + \sum_{k\geq 3} H_k(q_1, q_2, q_3, p_1, p_2, p_3), \quad (3.21)$$

where, as usual, H_k denotes a homogeneous polynomial of degree k.

We proceed as in the case of normal form above, but trying only to cancel all the terms such that the total degree in (q_1, p_1) is equal to 1. Using again complexification, as in the case of the normal form, for the couples (q_2, p_2) and (q_3, p_3), the current denominators to obtain the successive terms in the Hamiltonian G used to transform H are of the form

$$(k_1 - l_1)\lambda + \mathrm{i}\,(k_2 - l_2)\omega_1 + \mathrm{i}\,(k_3 - l_3)\omega_2,$$

with modulus bounded from below by $|\lambda|$, even if ω_1 and ω_2 are resonant. It is clear that, denoting the new variables as $Q_1, Q_2, Q_3, P_1, P_2, P_3$, if we set $Q_1 = P_1 = 0$ this is the desired centre manifold. Hence, setting these variables to zero we have a Hamiltonian with two d.o.f., which gives the reduction to the centre manifold of the initial Hamiltonian. The process is formal, there is no convergence in general, but one can obtain a good approximation in a suitable domain. One can check up to which distance of the fixed point the approximation satisfies some tolerance condition. See [42] for an example around the collinear point L_2 in the spatial circular restricted three-body problem.

3.3.5 Instability, bounds and detection

In the case of a Hamiltonian with $n \geq 3$ d.o.f., in principle, there is no way to avoid diffusion. The maximal dimensional tori have dimension n, that is, codimension $n-1$ in a fixed level of energy, and they do not separate the phase space. For instance,

initial conditions as close as we like to $L_{4,5}$ in the spatial circular restricted three-body problem (see the beginning of Section 3.4), which are totally elliptic fixed points, can go far away from these points. But normal forms, or averaging, lead to the so-called Nekhorosev estimates [37], showing that one needs an extremely large time if one starts close enough to the libration point. See also [14] for a rather detailed approach. Similar things happen for $(2n-2)$-dimensional symplectic maps.

Consider a perturbation $H(I,\varphi) = H_0(I) + \varepsilon H_1(I,\varphi,\varepsilon)$ of an integrable Hamiltonian H_0. The basic idea of the bounds is similar to the averaging Theorem 3.1.1, trying to cancel, around an arbitrary torus labelled by the action I^*, the dependence with respect to φ. But now the frequencies of the unperturbed Hamiltonian $\omega(I) = DH_0$ may not satisfy the DC and, on the other hand, the perturbation will produce that the frequencies change. Hence, the passage through resonances or through other frequencies not satisfying the DC is unavoidable.

First one should examine what is the effect of a resonance. We refer to Subsection 3.2.2 where we commented on the width associated to a pendulum like structure. A perturbation $\mathcal{O}(\varepsilon)$ can give rise to variations $\mathcal{O}(\sqrt{\varepsilon})$ due to the presence of a simple resonance. This happens if the frequencies change, reach a resonance and then go away from it. But then one can put the following question. Assume that in the variation of some action there is a term, due to the perturbation, like $\dot{I}_j = \varepsilon\cos((k,\varphi))$, where (k,φ) is a linear combination of the angles, and the related combination of the frequencies satisfies $(k,\omega) = 0$. One expects that the frequencies will change with time and one will escape from resonance, but it can happen that the *frequencies are locked at resonance up to order* m for some $m > 0$. That is, $\frac{d^k}{dt^k}(k,\omega) = 0$ for $k = 0,1,\ldots,m$, and $\frac{d^{m+1}}{dt^{m+1}}(k,\omega) \neq 0$. Then, during a long time, the term $\cos((k,\varphi))$ will be close to constant and the action can change by a large amount. If the locking occurs at all orders, the change in I_j will be $\mathcal{O}(\varepsilon t)$. To prevent this locking is why Nekhorosev introduced the so-called *steepness condition*, which prevents the order of the locking exceeding a maximal value. Then one has the Nekhorosev result: under steepness of some order, the variation of the actions $||I(t) - I(0)||$ does not exceed a bound $\mathcal{O}(\varepsilon^b)$ during a time interval $|t| < \mathcal{O}(\exp(c\varepsilon^{-a}))$, where the positive constants a, b, c depend on the order of steepness and properties of H_0, assuming that the norm of H_1 is bounded.

Around a given point, or a given torus (in particular, a periodic orbit) it can happen that there are many KAM tori. The above description of the Nekhorosev estimates puts a bound on how fast escap from the vicinity of these tori can be. Typically, one refers to this fact as *stickiness of the invariant tori*. Perhaps the escape is so slow that it has no relevance during the time interval in which we are interested, or even during the period of validity of the model. This suggests that we introduce the concept of *practical stability*. Assume that the studied object has $I = I^*$. Then, for fixed values of (ε, T), where ε is moderately small and T is large, we say that there is (ε, T)-practical stability if there exists $\rho = \rho(\varepsilon, T)$, such that points with initial conditions at $t = 0$ satisfying $||I(0) - I^*|| < \rho$ evolve with time

satisfying $||I(t) - I^*|| < \varepsilon$ for all $t \in [0, T]$; that is, we require stability only for finite time. See [14].

Clearly, for any v.f. with Lipschitz constant L, (ε, T)-practical stability is found if $\rho \leq \varepsilon \exp(-LT)$, as follows from Gronwall's Lemma. But this gives *extremely small* values of ρ, completely useless for any practical application. More realistic values would be $\rho = 0.01$ for $\varepsilon = 0.02$ and $T = 10^9$, depending on the practical example in mind. See, e.g., [9] for a nice approach to KAM and practical stability simultaneously.

Another relevant point is how to detect the existence of chaos and quantify it in a concrete example. There are many different approaches. We comment on the Lyapunov exponents.

To measure the instability properties of a fixed point (of a continuous or discrete system) it is enough to look at the differential of the v.f., or of the map at that point. How to proceed for a general orbit? The idea is to look for the rate of increase (if any) of the distance between the orbits of nearby points. In the limit, this becomes the rate of increase of an initial displacement, ξ, under the differential of the iterates of the map or under the action of the first order variational flow. For concreteness we consider the case of discrete maps.

Let x_0 be an initial point on a manifold $\mathcal{M}$ on which it acts a map F, and let $x_1 = F(x_0), \ldots, x_k = F(x_{k-1}), \ldots$ be the orbit of x_0. We can define, if it exists,

$$\Lambda = \sup_{\xi} \lim_{k \to \infty} \frac{\log(||DF^k(x_0)\xi||)}{k}, \tag{3.22}$$

where ξ is taken from the vectors with unit norm $||\xi|| = 1$ in $T_{x_0}\mathcal{M}$, the tangent space to $\mathcal{M}$ at the point x_0. One can prove that the limit in (3.22) exists for almost every $x_0 \in \mathcal{M}$ and for almost every $\xi \in T_{x_0}\mathcal{M}$, and it is known as *maximal Lyapunov exponent*.

In the Hamiltonian case (or in the symplectic one) it is easy to prove that, for initial points in invariant tori of maximal dimension, the limit exists and is equal to zero. Typically, $||DF^k(x_0)\xi||$ behaves linearly in k in that case, which gives the desired limit. For generic unstable orbits one expects positive values of Λ. The geometrical reason is clear: every time that the iterates pass close to an hyperbolic object, the unstable component will increase at a geometric rate. For an integrable system, if, for instance, unstable and stable manifolds coincide, when returning near the hyperbolic object, this expansion is canceled due to the iterations which occur close to the stable manifold. But the existence of transversal homoclinic (or heteroclinic points) prevents this from occurring.

One of the basic questions is how to have an estimate of the limit. In practice the number of iterations should be finite (and there is also the effect of round off, which is another issue). A simple approach is to proceed to the computation in (3.22) using a different presentation. Let us define the *Lyapunov sums* as follows. Let x_0, ξ_0 be the initial point and vector, and set $S_0 = 0$. Then, at the k-th iterate,

we use the following algorithm:

$$x_k = F(x_{k-1}), \quad \eta_k = DF(x_{k-1})\xi_{k-1}, \quad \xi_k = \eta_k/||\eta_k||, \quad S_k = S_{k-1} + \log(||\eta_k||). \tag{3.23}$$

Hence, we normalize the tangent vector after every step and add the log of the normalization to the current value of the sum S. It is clear that the limit slope of S_k, as a function of k, should coincide with Λ, as defined in (3.22). Hence, we can proceed as in (3.23) and, from time to time (say, after mN iterates, $m = 1, 2, \ldots$), fit a line to three different subsamples of the current sample (e.g., last 30%, last 50% and last 70%) and accept the average of the slopes as value of Λ if they differ by less than a prescribed tolerance. Otherwise, keep iterating until the next multiple of N, provided this does not exceed a maximal value.

A problem is that, in case $\Lambda = 0$, the convergence can be slow; for instance, $\log(k)/k$ is below 10^{-5} only for $k \geq 1,416,361$. An alternative approach, which tends in a faster way to the limit and also smoothes out the oscillations due to the quasiperiodic effects (in the case of orbits), can be found in [8]. One can look for the systematic use of that method in [25] for a family of 2D symplectic maps in $\mathbb{S}^2$. Another idea, if one is interested only in deciding whether the orbit is regular or chaotic, is to stop computations and consider the orbit as chaotic if S_k exceeds some threshold.

3.4 Applications to Celestial Mechanics

In this section we present several applications to illustrate theoretical and computational approaches to simple examples in Celestial Mechanics. One can have a look at slides (C), concerning the role of dynamical systems in Celestial Mechanics. Most of the applications deal with the restricted three-body problem (RTBP). We shortly recall it.

The RTBP studies the motion of a particle P_3 of negligible mass under the gravitational attraction of two massive bodies, P_1 and P_2, of masses m_1 and m_2, respectively. They are known as primaries or as primary and secondary. We assume that the primaries move in a plane along circular orbits around their centre of masses. We can normalize $m_1+m_2 = 1$ and $d(P_1, P_2) = 1$ and express the dynamics in a rotating frame (the so called synodical frame) with unit angular velocity. The problem depends on a unique parameter $\mu = m_2$. In this frame P_1 and P_2 are kept fixed at $(\mu, 0, 0)$ and $(\mu - 1, 0, 0)$.

The equations of motion are

$$\ddot{x} - 2\dot{y} = \Omega_x, \quad \ddot{y} + 2\dot{x} = \Omega_y, \quad \ddot{z} = \Omega_z, \tag{3.24}$$

where

$$\Omega(x, y, z) = \frac{1}{2}(x^2 + y^2) + \frac{1-\mu}{r_1} + \frac{\mu}{r_2} + \frac{\mu(1-\mu)}{2},$$

$r_1^2 = (x-\mu)^2 + y^2 + z^2$, and $r_2^2 = (x+1-\mu)^2 + y^2 + z^2$. The function

$$J(x, y, z, \dot{x}, \dot{y}, \dot{z}) = 2\Omega(x, y, z) - (\dot{x}^2 + \dot{y}^2 + \dot{z}^2)$$

is a first integral, its value being known as Jacobi constant and it is usually represented as C. The related 5D energy manifolds are defined as

$$\mathcal{M}(\mu, C) = \left\{(x, y, z, \dot{x}, \dot{y}, \dot{z}) \in \mathbb{R}^6 | J(x, y, z, \dot{x}, \dot{y}, \dot{z}) = C\right\} \tag{3.25}$$

and their projections on the configuration space are known as *Hill's regions*, bounded by the zero velocity surfaces (ZVS) (the zero velocity curves, ZVC, in the planar case).

The problem has five equilibrium points (also known as libration points):

(i) Three of them, say L_1, L_2 and L_3, are collinear (or Eulerian) on the x-axis, of centre×centre×saddle type and, hence, they have a 4D centre manifold which contains the so-called horizontal and vertical periodic orbits of Lyapunov type (to be denoted as hpo_L and vpo_L), invariant 2D tori and other periodic orbits (like the halo orbits, depending on the value of C), as well as chaotic regions.

(ii) Two of them, say L_4 and L_5, are triangular (or Lagrangian) at $x = \mu - 1/2$, $y = \pm\sqrt{3}/2$, $z = 0$. The term $\mu(1-\mu)/2$ in Ω is added to have $C(L_{4,5}) = 3$. Let μ_j be the value of μ for which the ratio of frequencies in the plane, $\left[(1 \pm (1 - 27\mu(1-\mu))^{1/2})/2\right]^{1/2}$, is j. The points are totally elliptic for $0 < \mu < \mu_1 = (9 - \sqrt{69})/18$ and the 2:1, 3:1 resonances (leading to instability) show up for $\mu_2 = (45 - \sqrt{1833})/90$ and $\mu_3 = (15 - \sqrt{213})/30$. Associated to the planar frequencies there are the so-called short and long period periodic orbits. The vertical frequency, giving rise also to a family of vpo_L, is equal to 1.

3.4.1 An elementary mission around L_1

First we consider the planar case. Assume that P_1 and P_2 are Sun and Earth, respectively. The distance between them, 1.5×10^8 km, and the period, 1 year, are scaled to 1 and 2π units, respectively, as said before and we take $\mu = 3.0404326 \times 10^{-6}$ (it includes Moon's mass). We want to carry out the following steps:

(i) Compute a periodic orbit of the system, around the Earth, with a period of 1 day (a geostationary orbit) and check that it is close to circular. Call it PO_1.

(ii) Compute some periodic orbits around L_1 (of the hpo_L family), which are symmetrical with respect to the x-axis. Check that they are unstable. We call them, in general, PO_2.

(iii) Compute the left branches of the stable manifolds of the previous orbits until they reach some suitable value of x (e.g., $x = -0.999$).

(iv) Now assume an spacecraft is moving in the "parking" orbit PO_1. At some point of the orbit we give an impulsion Δv, in the direction of the velocity at that point, with the goal of reaching a point of the stable manifold of one of the hpo_L. Determine the hpo_L which are reachable in that way from the parking orbit, at which place one should give the impulsion and which is the size Δv.

This allows us to obtain an elementary approach to a space mission. Later, one can consider the effect of perturbations of other bodies, the separate effects of Earth and Moon, change to a non-planar target orbit, the fact that the target orbit is, approximately, quasiperiodic instead of periodic, to optimize with respect to fuel consumption and with respect to transfer time from departure to a vicinity of the target orbit, etc. For information about the methodology for the design and control of missions around libration points see [15, 16, 17, 18]. We detail the steps to find the solution in the present example.

Step 1: First we compute a periodic orbit around the Earth with period $\tau = 2\pi/366.25$. We start with initial data $(x_0, 0, 0, \dot{y}_0)$ and require $\varphi_\tau(x_0, 0, 0, \dot{y}_0) = (x_0, 0, 0, \dot{y}_0)$. In fact, it is much simpler to ask for the image at $t = \tau/2$ to be of the form $(x_1, 0, 0, \dot{y}_1)$, and then symmetry completes the task. We have two known data $x_0, \dot{y}_0$ and two conditions $y_1 = 0$, $\dot{x}_1 = 0$. After a few attempts one can use Newton's method to find the solution $x_0 \approx -0.999714471273, \dot{y}_0 \approx 0.103463316596$. One can check that the monodromy matrix has a double eigenvalue equal to 1 (as expected: energy preservation and time shift) and the other eigenvalues are $\exp(\pm\alpha \mathrm{i}\,)$, $\alpha \approx 0.034228998$. The difference with respect to a circular orbit is less than 350 m. For further reference we denote this orbit as $\gamma(t)$.

Step 2: Now we face the hpo_L around L_1. First we locate L_1 by imposing $\Omega_x = 0$ as it follows from (3.24). Starting at $x = \mu - 1 + (\mu/3)^{1/3}$, Newton's method converges quickly for μ small. Then we can compute the eigenvalues at that point, which turn out to be λ, λ^{-1}, $\exp(\pm\omega \mathrm{i}\,)$, with $\lambda \approx 2.532659199$, $\omega \approx 2.086453579$. Hence, the maximal eigenvalue of the nearby periodic orbits, when they tend to L_1, is $\exp(2\pi\lambda/\omega) \approx 2052.671203$.

This large instability suggests, again, that we look for the initial data for the hpo_L on the Poincaré section $y = 0$ for a fixed x_0 with $\dot{x}_0 = 0$, and leaving $\dot{y}_0$ as the only unknown variable. The condition to be satisfied is then that the next intersection with $y = 0$ (to the left of L_1) should have $\dot{x} = 0$. This is easily solved by Newton's method. From the half orbit we recover the full orbit by symmetry, the monodromy matrix and, hence, dominant eigenvalue and eigenvector. The instability becomes milder when the size increases. For instance, for the smallest orbit in Figure 3.10 on the left the dominant eigenvalue is 2050.987058, while the largest one is 923.004416. Standard continuation techniques are used to generate these orbits.

Step 3: With the previously computed data it is simple to produce the left branches of the stable manifolds $W^{s,-}_{PO}$ of the hpo_L until they intersect the value $x = -0.999$.

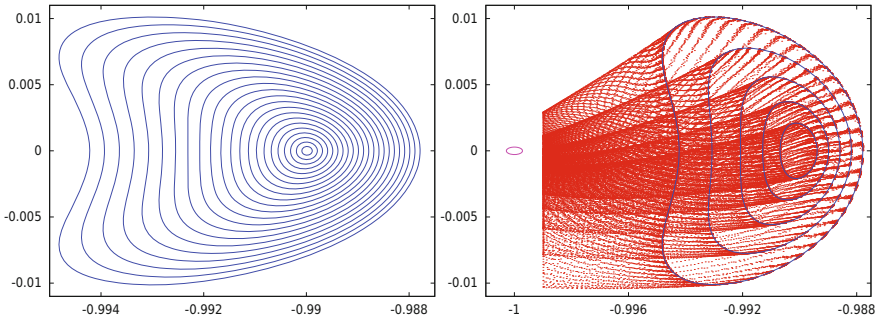

Figure 3.10: *Left:* some orbits in the family hpo_L around L_1. The initial values of x, on $y = 0$, are of the form $x_{L_1} + k \times 10^{-4}$ for $k = 1(1)22$. *Right:* For some of the orbits, concretely for $k = 6(4)22$, we plot also the left branches of $W^s_{PO_k}$ until they reach $x = -0.999$. In both plots the variables x, y are shown.

It is enough to use the linear approximation of the manifold in the Poincaré section $y = 0$. An example is shown in Figure 3.10 to the right. To compute the manifolds 200 points have been taken in a fundamental domain, equally spaced in logarithmic scale. The intersections for the orbits with $k = 8(2)22$, i.e., for the indices ranging from 8 to 22 with step 2 (see Figure 3.10) are shown in red in Figure 3.11 on the right, using $y, \dot{y}$ as variables.

Step 4: The last step is how to reach $W^{s,-}_{PO_k}$ for a given k leaving from the parking orbit. It is suggested to give an impulsion Δv from a given point $\gamma(t^*)$ in the orbit, in the direction of the velocity $\dot{\gamma}(t^*)$ at that point. The first question is to compute what is the size of the new velocity. We simply require that the value of the Jacobi constant with this velocity equals the one of the target PO_k. Let $|v|$ be the modulus obtained for this velocity. Then, $\Delta v = |v| - |\dot{\gamma}(t^*)|$, and the components of the new velocity are proportional to the ones of $\dot{\gamma}(t^*)$. This allows us to compute the trajectories $\psi(t, t^*)$ leaving from the parking orbit until they reach $x = -0.999$. Depending on t^* it can happen that $\psi(t, t^*)$ reaches $x = -0.999$ or it goes first far away to the left, spending too much time. These trajectories are skipped. A sample of the possible $\psi(t, t^*)$ trajectories for several t^* values is shown in magenta in Figure 3.11 on the left, where the parking and target orbit (with $k = 14$) are in red, and $W^{s,-}_{PO_{14}}$ is shown in blue.

Finally, on the right-hand part of Figure 3.11 we show, in the $(y, \dot{y})$ variables, the information that has been obtained in $x = -0.999$: the intersections of $W^{s,-}_{PO_k}$ for $k = 8(2)22$, in red, and the intersections of $\psi(t, t^*)$ when one changes t^*, for the Jacobi levels of PO_k, $k = 10(4)22$, in blue. The intersections of a given red curve with the corresponding blue one are the candidates for the transfer. The values of Δv are quite close. They range from 0.040286 for $k = 10$, to 0.041246 for $k = 22$ (i.e., impulsions ranging from 1.203 to 1.232 km/s).

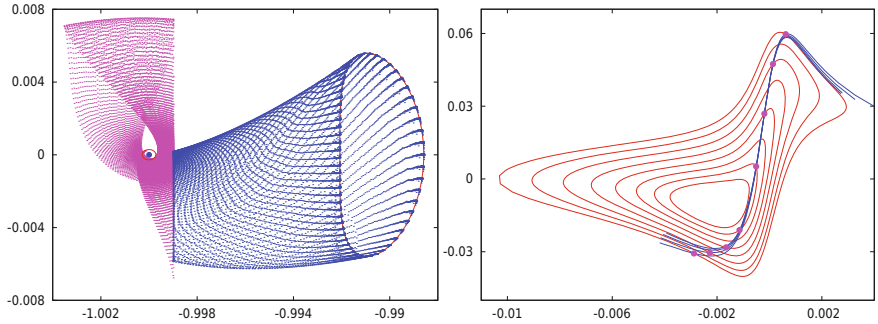

Figure 3.11: *Left:* The parking orbit and an example of a possible target hpo_L (with $k = 14$), both in red, the branch $W^{s,-}_{PO_{14}}$ in blue, and some of the possible trajectories $\psi(t, t^*)$ departing from the parking orbit (see text) in magenta. Plot done using x, y variables. *Right:* The intersections of $W^{s,-}_{PO_k}$ for $k = 8(2)22$ with $x = -0.999$, in red, and the intersections with the same plane of $\psi(t, t^*)$ for different values of t^* on the Jacobi levels of PO_k, $k = 10(4)22$, in blue. Note that these four blue curves are quite close and similar. The possible places for the transfer are the intersections of a $W^{s,-}_{PO_k}$ curve with the corresponding blue curve. They are marked in magenta. For each k shown here two possible places are obtained. This plot is done using $y, \dot{y}$ as variables.

3.4.2 Escape and confinement in the Sitnikov problem

This is an example to study escape/capture on a given problem of Celestial Mechanics using a very simple model. Two massive bodies of equal mass are moving on the $z = 0$ plane on elliptic orbits of eccentricity e around the common centre of mass, located at $(0, 0, 0)$, with semimajor axis $a = 1$, while a body of negligible mass moves along the z-axis. The standing equations are

$$\ddot{z} = -\frac{z}{(z^2 + r(t)^2/4)^{3/2}}, \quad r(t) = 1 - e\cos(E), \quad t = E - e\sin(E), \tag{3.26}$$

where E denotes the eccentric anomaly of the primaries. For $e = 0$ the problem has one d.o.f. and, hence, it is integrable. As a first order system we have $\dot{z} = v$, $\dot{v} = z(z^2 + r(t)^2/4)^{-3/2}$, with the obvious symmetries $S_1 \colon (z, v, t) \leftrightarrow (z, -v, -t)$, $S_2 \colon (z, v, t) \leftrightarrow (-z, v, -t)$, and $S_3 \colon (z, v, t) \leftrightarrow (-z, -v, t)$. We can introduce E as new time variable (denoting $' = d/dE$) and introduce a Hamiltonian formulation:

$$H(z, E, v, J) = (1 - e\cos(E))\left[\frac{1}{2}v^2 - (z^2 + (1 - e\cos(E))^2/4)^{-1/2}\right] - J.$$

A suitable Poincaré section for the representation of orbits is $\Sigma = \{z = 0\}$, using (v, E) as local coordinates. Thanks to the symmetry and to avoid strong deformations we shall use, instead, $(\hat{v}, E)$, where $\hat{v} = |v|(1 - e\cos(E))^{1/2}$.

If the infinitesimal mass escapes to infinity, the massive bodies move in $\mathbb{S}^1$ (eventually, after regularization of binary collisions using Levi–Civita variables).

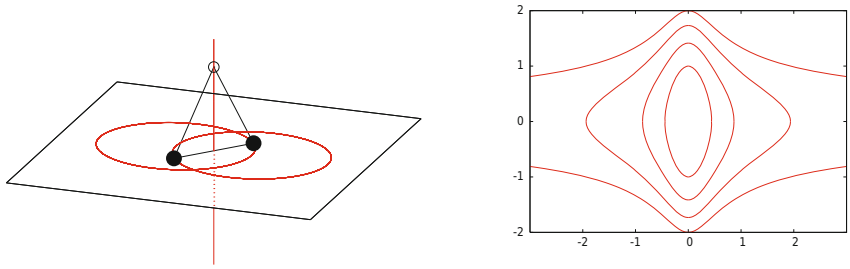

Figure 3.12: *Left:* A representation of the Sitnikov model. *Right:* For $e = 0$ plots of the orbits in the (z, v) variables for values of H equal to -1.5, -1.0, -0.5 and 0.

One talks of a periodic orbit at infinity. A celebrated Theorem by Moser states the following.

Theorem 3.4.1. *The problem has periodic orbits at both z plus and minus infinity, with invariant manifolds (orbits going to or coming from infinity parabolically). For e small enough the manifolds intersect Σ in curves diffeomorphic to circles. These curves have transversal intersection, implying the existence of heteroclinic orbits from $+\infty$ to $-\infty$ and vice-versa.*

As a consequence one has non-integrability, embedding of the shift with infinitely many symbols, existence of oscillatory solutions, escape/capture domains, etc. The PO at ∞ is parabolic or, topologically, weakly hyperbolic. The linearized map around the PO is the identity. To study the vicinity of these orbits we introduce McGehee variables (q, p) defined as $z = 2/q^2, \dot{z} = -p$. Then the equations of motion become

$$q' = \Psi q^3 p, \quad p' = \Psi q^4 \left(1 + \Psi^2 q^4\right)^{-3/2}, \quad \Psi = (1 - e\cos(E))/4. \tag{3.27}$$

If $e = 0$ the invariant manifolds are given as $p = \pm q(1 + q^4/16)^{-1/4}$. We shall denote as $W^{u,s}_{\pm}$ the intersections of unstable/stable manifolds of $\pm\infty$ with Σ. Due to S_3, $W^u_{\pm}$ coincide and also $W^s_{\pm}$ coincide, but W^s_+, W^u_- have $v > 0$, while W^s_-, W^u_+ have $v < 0$. Due to S_1, W^u_+ and W^s_- are symmetric with respect to $E = 0$.

We look for a parametric representation of the manifolds of the PO as

$$p(E, e, q) = \sum_{k\geq 1} b_k(e, E) q^k = \sum_{k\geq 1} \sum_{j\geq 0} \sum_{i\geq 0} c_{i,j,k} e^i \,\mathrm{sc}(jE)\, q^k, \tag{3.28}$$

where $b_k(e, E)$ are trigonometric polynomials in E with polynomial coefficients in e, $c_{i,j,k}$ are rational coefficients, and sc denotes sin or cos functions.

Note that the problem can be reduced to obtain invariant manifolds of fixed parabolic points of discrete maps (think about the intersection of the manifolds with $E = 0$). In this context McGehee proved that the invariant manifolds are

analytic except, perhaps, at $q = 0$, see [31]. In fact, a result of Baldomà and Haro [1] shows that, generically, the 1-dimensional manifolds of fixed parabolic points are of some Gevrey class (see the part on invariant manifolds in Section 3.2.1).

From (3.27) and (3.28) the invariance of the manifolds can be written as

$$\Psi q^4 \left(1 + \Psi^2 q^4\right)^{-3/2} = \sum_{k\geq 1} \frac{db_k}{dE}(e, E) q^k + \sum_{k\geq 1} b_k(e, E) \Psi k q^{k+2} \sum_{m\geq 1} b_m(e, E) q^m. \tag{3.29}$$

Equating coefficients of powers of q in (3.29) leads to the recurrence

$$\binom{-\frac{3}{2}}{m} \left(\frac{1 - e\cos(E)}{4}\right)^{2m+1} = b'_n(e, E) + \frac{1 - e\cos E}{4} \sum_{k=1}^{n-3} k b_k(e, E) b_{n-2-k}(e, E), \tag{3.30}$$

where $m = n/4 - 1$, defined only for n multiple of 4.

To solve the recurrence in (3.30) we first note that for the unstable manifold of $+\infty$ we have $b_1 = 1$. One has $b_1 = -1$ for the stable manifold. For a given value of n we can split the function b_n as $\tilde{b}_n + \bar{b}_n$, where $\bar{b}_n$ denotes the average and $\tilde{b}_n$ the periodic part. Given $b'_n(e, E)$ equal to some known function (computed from the previous coefficients) allows us only to compute the periodic part $\tilde{b}_n$. The average $\bar{b}_n$ is computed previous to the solution of the equation for $b'_{n+3}(e, E)$, to have a zero average function when we integrate. An essential fact is that $b_2 = b_3 = b_4 = 0$. One has also $b_6 = b_7 = b_{10} = 0$, but this is not so relevant.

Now it is a simple task to implement the computation of the coefficients to high order. Using high order is important, because this allows us to have a good representation for large values of q. A large q allows us to start the numerical integration, to obtain the intersection W^u_+ of the manifold with $z = 0$, at a moderate value of z. For instance, using terms up to order $n = 100$ one checks that the representation is good (error of the order of 10^{-16}) for $q = 1/3$. Then the numerical integration can be started at $z = 2/q^2 = 18$.

Figure 3.13 shows some results for different values of e, displaying W^u_+ and W^s_-, and using the $(\hat{v}, E)$ variables as polar coordinates. Note that the use of $(|v|, E)$ would give curves extremely elongated to the right for e close to 1. Concretely, if the eccentricity is equal to $1 - \delta$ then the horizontal variable in the plots reaches values $\approx 2/\sqrt{\delta}$. The values of the splitting angle at $E = 0$ and $E = \pi$ on the section Σ are shown as a function of e in Figure 3.14. Note the quite different behaviour when $e \to 1$. This gives evidence of the transversality for all values of e.

Summarizing, the steps to obtain the manifolds W^u_+ and W^s_- and, hence, the splitting angle, are the following:

(i) introduce McGehee coordinates to pass from (3.26) to a formulation around the periodic orbits at infinity, as given by (3.27);

(ii) look for a suitable representation, as the one in (3.28), in which the manifold is expressed as function of a distance to infinity (q) and a periodic time variable

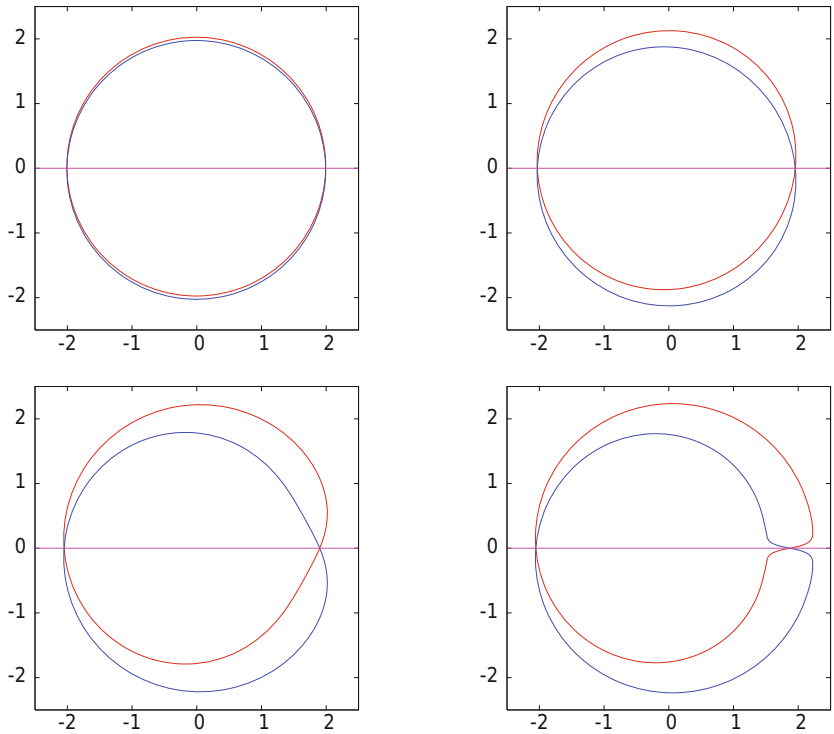

Figure 3.13: The manifolds W^u_+, in red, and W^s_-, in blue, for different values of e. *Top left:* for $e = 0.1$. *Top right:* for $e = 0.5$. *Bottom left:* for $e = 0.9$. *Bottom right:* for $e = 0.999$. In all cases we use $(\hat{v}, E)$ as polar coordinates.

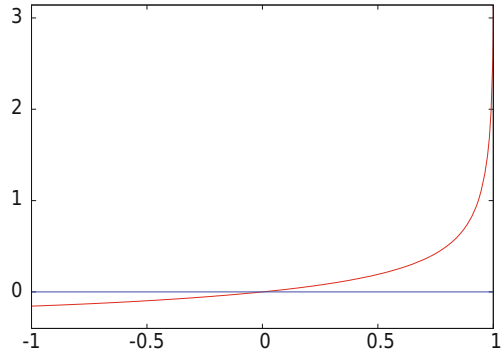

Figure 3.14: The splitting angle of the manifolds W^u_+ and W^s_- in Σ. For positive values on the horizontal axis the splitting angle at $E = 0$ is shown as a function of e. For the negative ones, the splitting angle at $E = \pi$ is shown as a function of $-e$.

(E); write the invariance condition (3.29) and derive the recurrences, as given in (3.30);

(iii) analyze the properties of the recurrences (symmetries, powers of e in the coefficients of the trigonometric polynomials, etc); design and implement routines to obtain the desired numerical coefficients; and

(iv) select a suitable value of q for the current maximal order of the expansion, evaluate (3.28) for a sample of values of E for every desired value of e, and carry out the numerical continuation until $z = 0$.

It is important to stress that, for other similar problems (RTBP planar or spatial, general, etc), to decide if an observed body will be captured or will escape, it is enough to obtain the manifolds and decide the actual position with respect to them. The case of the planar RTBP with a comparison between theoretical predictions and numerical results can be found in [28] and the related slides (I).

3.4.3 Practical confinement around triangular points

As mentioned at the beginning of Section 3.4, the triangular libration points are linearly stable in the 3D RTBP if μ is small enough. But, what can be said about nonlinear stability? For the 2D case, nonlinear stability is proved for $\mu \in [0, \mu_1)$ except for the couple of values μ_2, μ_3. A possible approach is to reduce to the study of a symplectic 2D map and to apply Moser theorem. There is an exceptional value for which the twist condition is not satisfied, but can be recovered as a *weak twist* to higher order via normal forms.

In the 3D case, in principle, there is no way to avoid diffusion. Hence, initial conditions as close as we like to $L_{4,5}$ can go far away from that point. But normal forms, or averaging, lead to the already mentioned Nekhorosev estimates, showing that one needs an extremely large time if one starts close enough to the libration point as discussed in Subsection 3.3.5.

But these results, concerning domains of practical stability in the 3D case, give at most small regions around the triangular points. On the other hand one has found the so-called Trojan (and Greek) asteroids, for the Sun-Jupiter system, far away from $L_{4,5}$, even with relatively high inclination. Hence, it seems that the domain of practical stability for long times is much larger than what is given by theoretical predictions. It would be nice to search for the confining mechanisms.

A side problem is why Trojan-like bodies are not found in the Earth-Moon case. Certainly the Sun is guilty for that, the orbits equivalent to $L_{4,5}$ for the Earth-Moon system being unstable even in simple models of the Earth-Moon-Sun motion. But this does not exclude the possibility that stable orbits exist with moderate inclination.

Here we present some results which can help to understand the main mechanisms, see [48]. For different reasons, many computations are done with initial

conditions on the ZVS using (z, α, ρ) as parameters for a fixed μ, as follows:

$$x = \mu + (1+\rho)\cos(2\pi\alpha), \quad y = (1+\rho)\sin(2\pi\alpha), \quad z = z_0 \geq 0, \quad \alpha \in (0, 1/2),$$
$$\dot{x} = \dot{y} = \dot{z} = 0. \tag{3.31}$$

As for $\mu = 0$ one must be in $1-1$ resonance, it is convenient to look, starting at the ZVS, for initial conditions at rest, in the synodical frame, in the moment that an elliptic orbit with semimajor axis equal to the unity passes through the apocentre in the sidereal frame. That is, for values of $(z, R = 1+\rho)$ related by

$$\begin{gathered} z = \left[4(1+R^2)^{-2} - R^2\right]^{1/2} \quad \text{or} \\ \psi = 1 - \tfrac{1}{2}w + \tfrac{3}{2^5}w^2 - \tfrac{1}{2^8}w^3 - \tfrac{25}{2^{13}}w^4 + \tfrac{33}{2^{16}}w^5 + \mathcal{O}(w^6), \end{gathered} \tag{3.32}$$

where $w = z^2$, $\psi = \psi(z) = R^2$. This suggests that we make plots using the variables

$$(\alpha,\ \gamma = 1 + \rho - \sqrt{\psi(z)},\ z). \tag{3.33}$$

It is clear that L_5 corresponds to $\rho = 0$, $\alpha = 1/3$, $z = 0$. By symmetry, similar results are obtained for L_4. Also, by symmetry, it is enough to look for $z \geq 0$. For the limit case, $\mu = 0$, one would have $\gamma = 0$.

Some reasons to start at the ZVS are:

(i) Most of the i.c. non-leading to escape are on 3D tori. Hence, we scan a set of positive measure in the full phase space (not fixing the Jacobi constant C).

(ii) The results obtained can be used as a seed to obtain the relevant objects involved in the practical confinement, either starting at the ZVS or not.

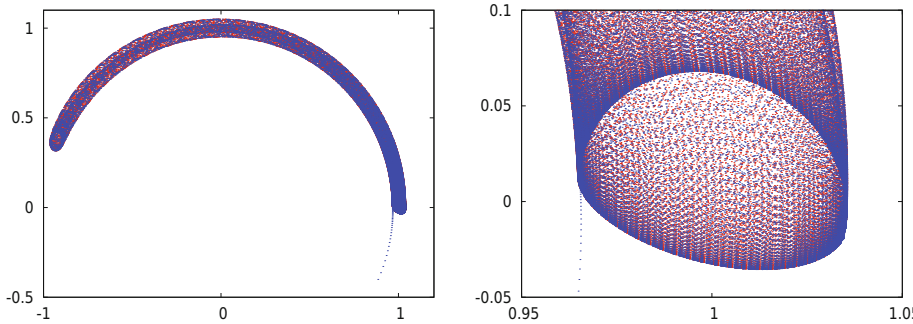

Figure 3.15: Example of a transition for $\mu = 0.0001$, $\alpha = 0.05$, $z = 0.3$. The two tori (confined in red, escaping in blue) have values of ρ which differ in 10^{-10}. We show the projections on (x, y) of the Poincaré section through $z = 0$. *Left:* a global view. *Right:* a magnification. The separating unstable 2D torus or invariant curve in the section belongs to $W^{u,s}_{L_3}$. Note that the points in red are partially hidden by the ones in blue.

First, we show some results concerning the *quasi-boundary* between escape and practical confinement. Figures 3.15 and 3.16 display, for a small value $\mu = 10^{-4}$ of the mass parameter, two different kinds of objects which appear on the quasi-boundary. We should mention that the relevant objects have codimension 1 in the full phase space. In the present case they have dimension 5. Typically, they are $W^{u,s}$ of central objects of dimension 4. These objects can be the centre manifolds of fixed points of centre×centre×saddle type or the centre manifolds of 1-parameter families of periodic orbits of centre×saddle type (the parameter being, e.g., the value of the Jacobi constant). But it is clear that these $W^{u,s}$ do not coincide: there is some splitting. This is the reason why they are named quasi-boundaries.

We note, for instance, that in the upper left plot of Figure 3.16 beyond the blue curve commented on the caption, one can guess another invariant curve (in the Poincaré section, a 2D torus in the phase space) on top of the plot. The separation between confined and escaping orbits is close to a double heteroclinic connection between the lower curve in blue and the upper one in red. But the related branches of these two partially normally invariant curves do not match exactly. There is some tiny splitting between the branches.

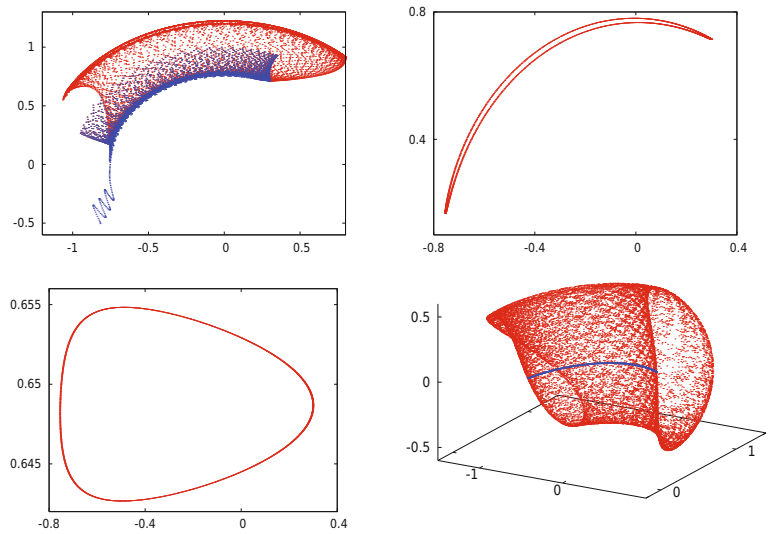

Figure 3.16: Similar to Figure 3.15 but starting at $\alpha = 0.4$, $z = 0.6$. Now the separating unstable 2D tori are not in $W^{u,s}_{L_3}$. *Top:* initial part of Poincaré iterates with many iterates in blue, giving evidence of the lower unstable 2D torus and points escaping from it (*left*), and the separating lower unstable invariant curve alone (*right*) projected on (x, y). *Bottom:* The same curve projected on $(x, \dot{x})$ (*left*), and the related 2D separating unstable torus in a (x, y, z) projection (*right*).

In Figure 3.17 we display a general view of the boundary. See comments on the caption. Typically, the transitions have been detected after a maximum

integration time equal to $10^6 \times 2\pi$ (in special cases 10, 10^2 or 10^3 times larger) and with a resolution of 10^{-6} in ρ; see slides (D) for other values of μ.

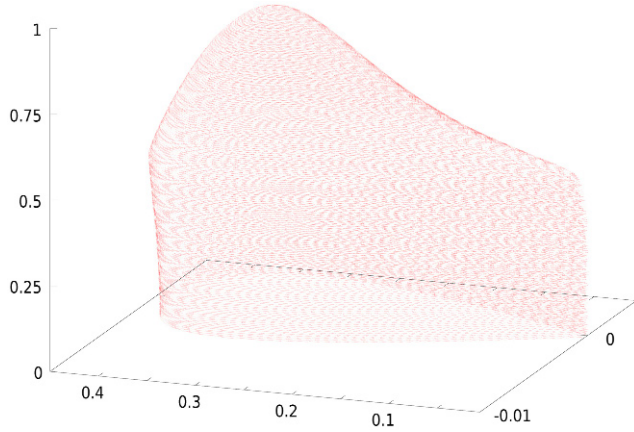

Figure 3.17: A 3D view of the detected boundaries of practical stability starting at the ZVS for $\mu = 10^{-4}$, shown in the (α, γ, z) variables. The inner (resp., outer) part corresponds to $\gamma < 0$ (resp. $\gamma = 0$). Note the sharp change on the behaviour of the boundary which occurs between $z = 0.4$ and $z = 0.5$.

We can make a rough scan of the boundaries for different values of μ, both for the planar and spatial RTBP. We say rough in the sense that, typically, the maximal time to look for escaping has been reduced to $10^5 \times 2\pi$ time units and that the grid we scan uses $\Delta\rho = 10^{-4}$, then $\Delta\alpha$ equal to 2×10^{-4} in the planar case (5×10^{-4} in the spatial one) and $\Delta z = 5 \times 10^{-3}$ in the spatial case. The results are shown in Figure 3.18. Note that the effect of the resonances is less important in the spatial case. This is due to the fact that, for some values of μ, the resonances destroy stability in the planar case, but still a large set of initial conditions is stable in the spatial case. The change of the frequencies when z increases is responsible for the minima being shifted to larger values of μ.

From now on we concentrate on a fixed value $\mu = 0.0002$. The reasons for this choice are the following:

(i) μ being small, the boundaries are sharper;

(ii) it should be also possible to obtain some information by means of perturbation theory;

(iii) it is close to the Titan-Saturn mass ratio.

This small value of μ, however, raises a problem: the escape is relatively slow and, hence, the integration time is large. The methodology used (for the L_5 case) is as follows:

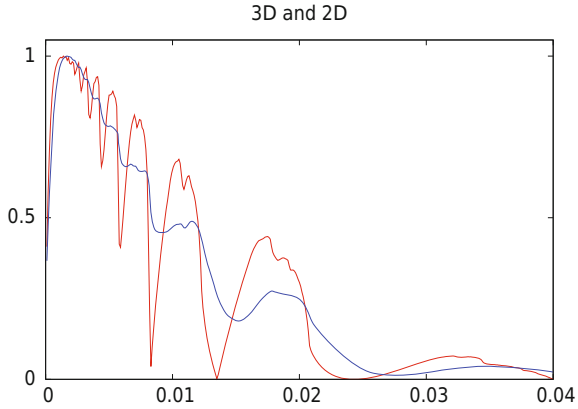

Figure 3.18: Statistics as a function of μ starting at the ZVC (planar case, in red) and at the ZVS (spatial case, in blue). This is normalized to the maximum, which for the planar case occurs at $\mu = 0.0014$ with 282757 points, and for the spatial case it occurs for $\mu = 0.0017$ with 19014882 points. Note the sharp effect of the resonances in the planar case. Similar patterns are found for the Hénon map and in many other examples, see [46]. In the spatial case the effect of the resonances is milder and delayed. In both cases some stability subsists even for $\mu > \mu_1$.

(i) Define some escape criterion (e.g., the (x, y) projection of the orbit enters some wedge near the negative y-axis, or the orbit comes too close or too far from the primary, or too close to the secondary).

(ii) Scan a set of initial conditions for short time (e.g., $10^4 \times 2\pi$, using some grid with small steps $\Delta\alpha$, $\Delta\rho$, δz). Look at every initial point on the grid, for fixed z, as a pixel. Keep the pixels non leading to escape.

(iii) Repeat for longer time (e.g., $5 \times 10^4 \times 2\pi$) for the pixels at a distance (counted in the sup norm) less than d pixel units from the ones which already escaped (typically, we take $d = 5$). The tested points are marked depending on whether they escape or they remain. Iterate the scan until no more points have to be tested: all the ones at distance less than or equal to d from escaping points have been tested and remain. Repeat two more times for longer and longer integration time ($25 \times 10^4 \times 2\pi$, $10^6 \times 2\pi$).

(iv) Eventually do additional refinements of ρ for fixed α, z.

Figures 3.19 and 3.20 show some results for $\mu = 0.0002$ displaying, for different values of z, the set of non-escaping points starting on the ZVS and the boundaries of the domain. See the captions for the variables used to represent the results. Note that the domain of practical stability contains, for the planar case $z = 0$, stable points quite close to the L_3 ($\alpha \approx 0$). In the spatial case there are stable orbits which reach z as large as 0.865 and, as the value of ρ for these orbits reaches ≈ -0.181 they have a maximum inclination exceeding 46 degrees.

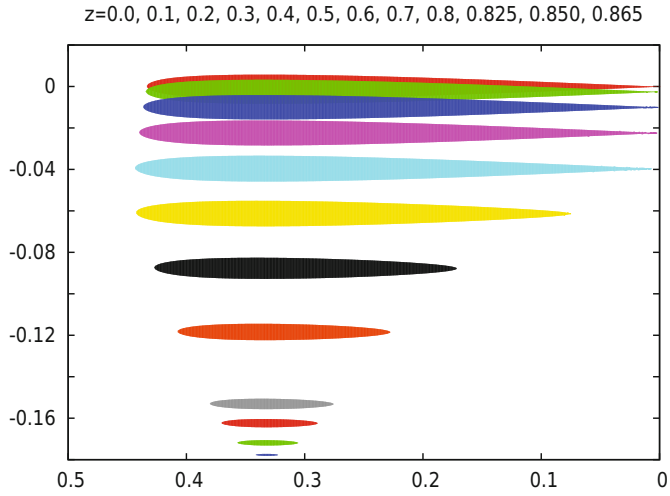

Figure 3.19: For $\mu = 0.0002$ the subsisting points, starting at the ZVS for 12 different z values, given on the top of the plot. The coordinates used for the representation are (α, ρ).

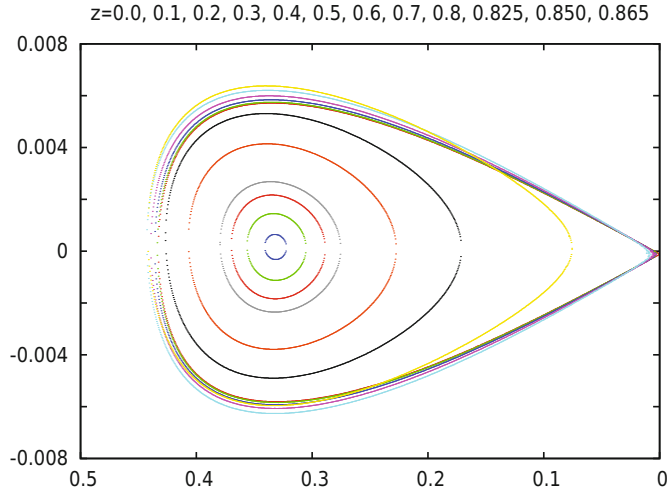

Figure 3.20: Boundaries of the domains shown in Figure 3.19 using the paraboloid like corrections. That is, as vertical variable one has used γ, as defined in (3.33) instead of ρ.

Some sections of the boundary for $\mu = 0.0002$, for several values of α, are shown in Figure 3.21.

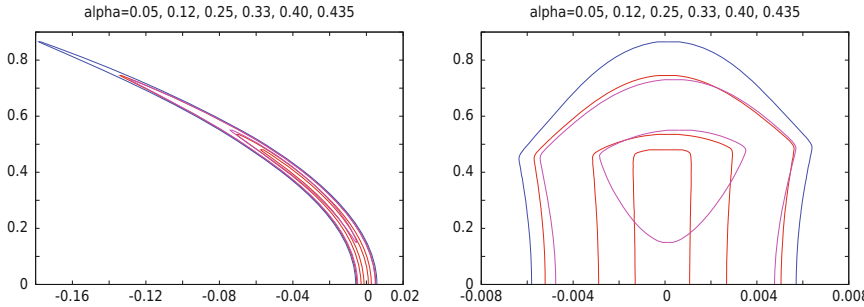

Figure 3.21: Some sections of the boundary starting at the ZVS for different values of α. *Left:* in the (ρ, z) variables. *Right:* using the (γ, z) variables. The curves for $\alpha = 0.05, 0.12, 0.25$ are plotted in red, and are easily seen on the right-hand plot going away from $(0, 0)$ and each line encircling the previous one. The curve for $\alpha = 0.33$ is displayed in blue. This is the largest one. Finally the curves for $\alpha = 0.40$ and $\alpha = 0.435$ are plotted in magenta. Last one does not reach $z = 0$.

Still many things must be completed even for this small μ for which the boundaries tend to be rather sharp, because they are associated to relatively small splitting. The problem becomes more rough for the Sun-Jupiter case, because then one starts to see the effect of some island-like structure. For the Earth-Moon case the behaviour is quite wild due to the strong effect of resonances. The Earth-Moon mass ratio is not far from the 3:1 resonance value μ_3.

3.4.4 Infinitely many choreographies in the three-body problem

In the Newtonian N-body problem with all masses equal to 1, we can consider very simple solutions in the planar case, the like N-gon relative equilibrium solutions. Due to the homogeneity one can scale time and distance so that it is enough to consider solutions with period 2π. The N bodies move on a circle of radius R such that

$$2R^3 = \Sigma_{j=1}^{N-1} (2\sin(j\pi/N))^{-2}.$$

It is clear that all the bodies move on the same path in the plane. Hence, the following is a natural question: are there other periodic solutions such that all bodies with equal masses move on the plane along the same path? At the end of the twentieth century a solution with 3 bodies on the same planar curve, different form a circle, was proved to exist by Chenciner–Montgomery [6]. Also, Moore [33] found the same orbit in a previous numerical work in a different context, a few years before. The path of this solution is the very popular figure eight curve and is displayed in Figure 3.22.

Immediately, one can pose the question for $N > 3$ and for other shapes of the path. These solutions are called *choreographies* because of the dancing-like

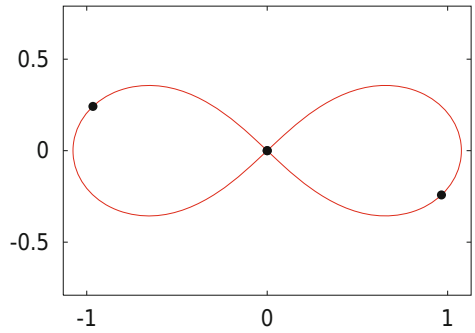

Figure 3.22: The figure eight solution of the three-body problem. The initial positions of the bodies are marked as black points. For concreteness, we can assume that at $t = 0$ the body located at the origin moves to the right, up. This forces the motion of the other two.

motion of the bodies seen in animations, see [5, 45]. More precisely, they should be called *simple* choreographies because they are on the same curve; we use the term *k-choreographies* for bodies moving on k different curves. Slides (F) provide some examples and links to animations. One can also introduce the notion of *relative* choreographies if they are seen as choreographies in a uniformly rotating frame. Two choreographies which differ only by a rotation, by scaling, change of orientation, symmetry, etc, should be seen as the same.

Returning to simple choreographies in a fixed frame (or *absolute* choreographies) what one tries to find is some 2π–periodic function $\psi\colon \mathbb{S}^1 \mapsto \mathbb{R}^2$ such that if the body j is located at $q_j(t) = \psi(t - (j-1)2\pi/N)$ for $j = 1, \ldots, N$, we have a solution to the equations of motion.

Another natural question arises: are there other choreographies of the three-body problem different from the figure eight?

A simple observation is that at some $t > 0$, relatively small, the three bodies in Figure 3.22 will be in an isosceles configuration. Such a configuration is defined, for instance, assuming that at some moment of time the bodies 2 and 3 have positions and velocities given by

$$x_3 = x_2, \quad y_3 = -y_2, \quad \dot{x}_3 = -\dot{x}_2, \quad \dot{y}_3 = \dot{y}_2. \tag{3.34}$$

The conditions for m_1 are determined from the centre of mass integrals. This isosceles triangle has a symmetry axis passing through m_1.

Assume that after some time τ the bodies pass through another isosceles configuration, concerning positions, with the body m_2 in the symmetry axis defined by the positions of m_3 and m_1, and that the velocities are close to satisfy the isosceles condition. Let β be the angle between the former symmetry axis (the x-axis) and the new one. A refinement is done to satisfy the full isosceles conditions

with good accuracy (see the end of this subsection). Then, after rotating positions and velocities at τ by an angle $-\beta$, we have an isosceles configuration with the same symmetries concerning velocities than the initial one. The only change is a circular permutation of the bodies with change of orientation. Then the action of the semi-direct product of $\mathbb{Z}_2$ and $\mathbb{Z}_3$ (symmetry and permutation of the bodies) produces a relative choreography with period $T = 6\tau$ and rotation 6β. If β is $k\pi, k \in \mathbb{Z}$, we have an absolute choreography, symmetric with respect to the x-axis.

This has been applied to $\approx 10^9$ initial conditions. Near 3×10^5 relative choreographies have been found and, by continuation of each one of them with respect to the angular momentum, many (345 up to now) absolute, non-equivalent, choreographies have been found. It is clear that several relative choreographies can lead, by continuation, to an absolute choreography equivalent to another one found previously, and these are not counted. It is checked that some of these new three-body choreographies seem to belong to families. An example is shown in Figure 3.23. See [44] for other families.

Figure 3.23 suggests to try to continue the family for an increasing number of loops. Now the continuation has to be done with respect to integers and not in a continuous way. But using extrapolation of the data from the previous loops it has been possible to continue the family without any problem (using quadruple precision and high order extrapolation) until the solution shown in Figure 3.24. The natural conjecture is that there are infinitely many choreographies in this family.

There is an easy description of that solution. One of the bodies (say, the red one) moves close to an elongated ellipse while the other two (green and blue) move in a close binary, with its centre of mass close to an ellipse. When the three bodies approach the centre of mass there is an exchange: the blue body moves close to an elongated ellipse and the red and green form a binary in turn. At the end of this we have traveled 1/3 of the period. The bodies return to the initial position with a cyclic permutation RGB $\to$ GBR. One should stress that when they approach the centre of mass the bodies are not close to triple collision. Preliminary results seem to indicate that the minimal value of the moment of inertia along the orbit is strictly decreasing with the number of binary loops, tending to a positive constant.

It should be mentioned that, among the 345 absolute choreographies available, one can identify several families. It is not excluded that some of these families contain infinitely many elements. But it can also happen that a couple of families merge together in a saddle-node bifurcation.

The steps for that application are as follows:

(i) To obtain initial data in isosceles configuration one can prescribe some negative energy. Then we give values of (x_2, y_2) and determine the positions of the other masses. Because of the symmetries we can select $x_2 > 0$, $y_2 < 0$. A bound on the domain is obtained because the kinetic energy should be

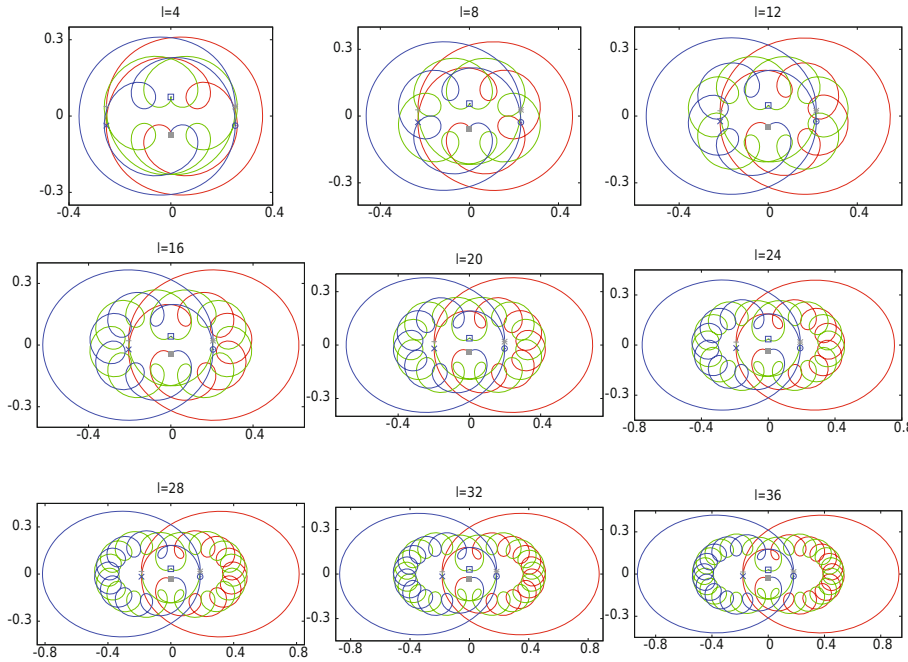

Figure 3.23: Choreographies of the three-body problem belonging to a family. The paths of the three bodies during 1/3 of the period are shown in different colors. The positions of the bodies in the initial isosceles configuration and the ones after 1/6 of the period are also shown. To display the solutions with the same scale in x and y variables, the coordinates have been exchanged. Now, for these choreographies, the symmetry axis is the vertical one and for this family both isosceles configuration (at $t = 0$ and after 1/6 of the period) are symmetrical the one from the other with respect to the horizontal axis. Counting the little inner loops (for instance, the ones in red) the number increases from 1 to 9 from top to bottom and from left to right. The value ℓ on top of each plot refers to the total number of small loops, either in red, blue or green.

non-negative. The possible values of $(\dot{x}_2, \dot{y}_2)$ are parametrized by an angle $\gamma \in [0, 2\pi]$.

(ii) Then, we proceed to the integration of (3.1) with the selected initial conditions, looking for a passage near another isosceles configuration. A maximal time is used (e.g., 5 units) and the attempt is stopped if the bodies move too far or they become too close. If a candidate is obtained a refinement is done by Newton's method, to have a good approximation to an isosceles symmetry after 1/6 of the period. For the refinement we fix γ and leave (x_2, y_2) as free variables to satisfy the isosceles condition for the velocities when it is satisfied by the positions.

(iii) Next we carry out continuation by changing the angular momentum, looking

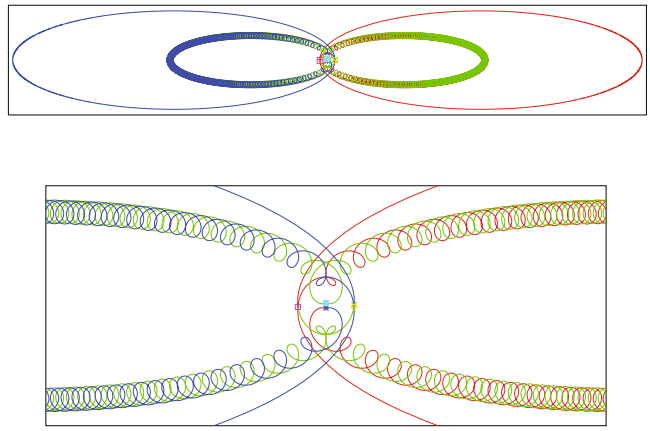

Figure 3.24: *Top:* a choreography of the three-body problem of the same family of the ones shown in Figure 3.23. In each of the binary portions the bodies in the binary make 200 revolutions around the centre of mass of the binary, while the third body moves close to an elongated ellipse. Only 1/3 of the orbit is shown. The remaining parts are obtained by cyclic permutations. *Bottom:* a magnification of the central part of the top.

for an absolute choreography. Continuation is stopped if the bodies approach a collision. The new absolute choreographies are stored in a list. If they are already in the list, they are discarded. Later, for our present goal, we select the ones which belong to the family as shown in Figure 3.23.

(iv) Finally the family is continued with respect to the number of loops. An extrapolation based on the previously computed loops allows us to have a very good guess. Newton's method converges in few iterations.

3.4.5 Evidences of diffusion related to the centre manifold of L_3

In this last application we consider the 3D RTBP for a small value $\mu = 0.0002$, like we used in Subsection 3.4.3. Our goal is to give evidence of the diffusion when we consider the unstable dynamics originated by the unstable/stable manifolds of the part $W^c_{L_3,C}$ of the centre manifold $W^c_{L_3}$ of L_3, for a given value C of the Jacobi constant. For concreteness, we use the value $C = 2.95998466228$. To have a feeling of the meaning, let us say that for that value of C the vpo_L in $W^c_{L_3,C}$ has values of z going from -0.2 to $+0.2$.

Beyond the vpo_L, the $W^c_{L_3,C}$ contains 2D tori, the hpo_L, some tiny chaotic domains, and the additional periodic orbits related to these domains. Using the methods of Subsections 3.3.1 and 3.3.3, we can compute both periodic orbits and several tori. It is simpler to represent the tori as ICs of the Poincaré map $\mathcal{P}$ associated to the section $\Sigma := \{z = 0, \dot{z} > 0\}$. In this application we shall use once and again Σ and $\mathcal{P}$. As we fixed also the value of C, we have to consider a discrete

map in a 4D space that we denote as Σ_C.

The ICs are hyperbolic normally to the centre manifold. Hence, we can compute its manifolds, say $W^u_{\mathcal{C}}$, $W^s_{\mathcal{C}}$, for a given curve $\mathcal{C}$. Note that these manifolds are 2D and to visualize them we can compute a section through some codimension-1 manifold in Σ_C (e.g., an hyperplane Π). A suitably chosen Π gives as $W^u_{\mathcal{C}} \cap \Pi$ a closed curve, say $\mathcal{C}_u$. In a similar way we can obtain $\mathcal{C}_s$. Of course, these two curves in $\Sigma_C \cap \Pi$, which is 3D, do not intersect generically, as opposite to $W^u_{\mathcal{C}}$ and $W^s_{\mathcal{C}}$ which are 2D in the 4D space Σ_C, for which one expects to have intersections, but not necessarily located in Π. But we can have a feeling of their relative position by looking at $\mathcal{C}_u$ and $\mathcal{C}_s$.

Figure 3.25 illustrates what has been said. In the left plot several ICs are shown, as well as the point corresponding to the vpo_L. Note that the largest IC is quite close to the hpo_L. The 2D torus corresponding to this last IC has values of z which range in the small interval $[-0.017, 0.017]$. The hpo_L, which is contained in $z = 0$, is located outside the largest IC shown at a distance ≈ 0.004. The right plot displays $\mathcal{C}_u$ and $\mathcal{C}_s$ for several ICs, using as Π the hyperplane defined by $y = -\sqrt{3}(x - \mu)$. One detects, visually, that for tori close to the vpo_L the curves are quite close. The difference increases going outside, away from the vpo_L, and decreases again when approaching the hpo_L. This will be one of the relevant facts to explain the results obtained.

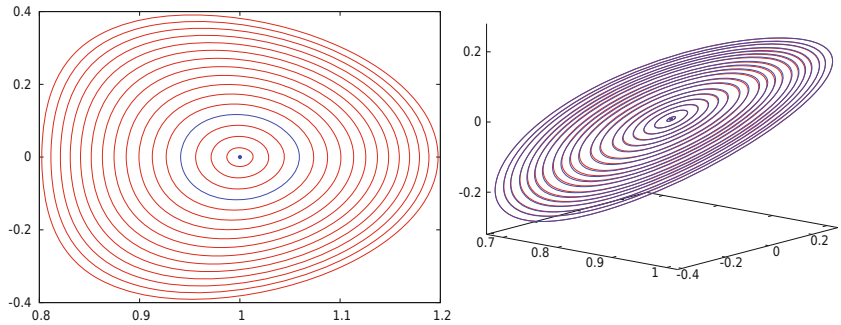

Figure 3.25: *Left:* invariant curves obtained as intersections with Σ of some tori in the $W^c_{L_3,C}$ for $C = 2.95998466228$ projected on the (x, y)-plane. The vpo_L orbit for this value of C has $z \in [-0.2, 0.2]$ and corresponds to the blue point. The blue curve will be used in the computations reported here. *Right:* sections with $y = -\sqrt{3}(x - \mu)$ of the Poincaré sections of the unstable (red) and stable (blue) manifolds of some of the tori. For the 3D view we use the $(y, \dot{y}, \dot{z})$ variables.

Figure 3.26 shows the projection in (x, y) of the first 10^5 iterates under $\mathcal{P}$ starting at a point close to the blue curve, say $\mathcal{C}_b$, in Figure 3.25, left. The first iterates follow closely the upper part of $W^u_{\mathcal{C}_b}$ and return near $\mathcal{C}_b$ close to the upper part of $W^s_{\mathcal{C}_b}$ (or of some other nearby curve). As it is well known, next iterates can continue going up or down, as happens after every return near $\mathcal{C}_b$, in a quasirandom

way. For completeness, the manifolds of vpo_L are also shown (displayed in blue).

This behaviour suggests that, at the successive returns near $W^c_{L_3,C}$, the Poincaré iterates can approach different tori (2D in the phase space) on that centre manifold. That is, a typical mechanism of diffusion thanks to chains of heteroclinic connections of different tori.

But there are also tori (3D for the Hamiltonian flow, 2D for $\mathcal{P}$) close to these manifolds. Among these tori one finds the ones close to the boundary of the practical stability domain for L_5, as seen in Subsection 3.4.3. Looking at Figure 3.19 one checks that they reach values of α very close to 0 (the value of α for L_3) up to $z = 0.4$. The successive points can remain for a large number of iterations, say 10^6 and even 10^8 in some tests, close to one of these tori, to one of the tori in the symmetric domain around L_4, or even tori which visit a vicinity of both L_5 and L_4 (with an (x, y) projection of the iterates in Σ similar to the red points in Figure 3.26). The tori are very sticky, see Subsection 3.3.5. As a consequence, the orbit of a point should consist of passages from the vicinity of the W^u of one of the ICs to the vicinity of the W^s of another IC (or, perhaps, the same one) with long stays near tori of one of the three types described.

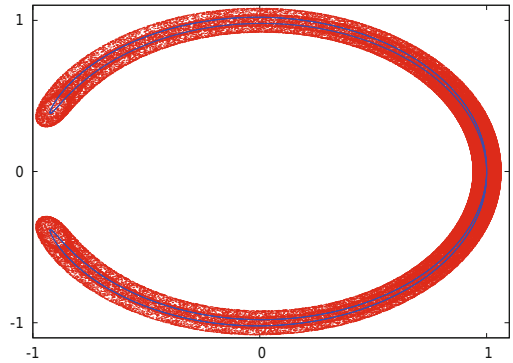

Figure 3.26: Starting at a point very close to the invariant curve in blue in Figure 3.25 we have computed the first 10^5 intersections with Σ. The plot shows the projections on the (x, y)-plane. As a reference, we also show in blue the initial part of the manifolds of the vpo_L. The lack of coincidence of these last manifolds is not seen with the present resolution.

To have evidence of this expected behaviour, we have taken 1920 points close to $\mathcal{C}_b$ (the blue curve in Figure 3.25 left). For every initial point we record the first 5×10^6 Poincaré iterates, except if some kind of escape is detected. A typical escape occurs when, going the iterates to the left, either near the upper or lower part of Figure 3.26, they approach the location of the secondary. After this encounter, the successive iterates can move close to the primary, escape far away or even return several times near the secondary. Anyway, only for 37 of the 1920 initial conditions escape was detected. Certainly the initial conditions will lead to escape if the number of Poincaré iterates is largely increased, at least on this level of the

Jacobi constant. See later for some tests with initial data taken near the vpo_L.

To visualize the diffusion and to display a moderate amount of data we have computed passages of the Poincaré iterates through a narrow slice around $x = 0$. Only from time to time an iterate falls in the slice. For instance, among the $1920 \times 5 \times 10^6$ computed Poincaré iterates (and except for the few iterates lost because of escape) only $\approx 3.2 \times 10^6$ fall in the slice $|x| < 10^{-3}$. The passage can occur in the upper part going from right to left (inner transition) or from left to right (outer transition), and also from right to left (outer transition) or from left to right (inner transition) in the lower part (see Figure 3.26).

The variables used in Σ are $(x, y, \dot{x}, \dot{y})$. Due to the symmetries, the inner upper and inner lower transitions are symmetrical, with the changes $(x, y, \dot{x}, \dot{y}) \leftrightarrow (x, -y, -\dot{x}, \dot{y})$, and the same occurs for the outer ones.

Using only the points falling into the slice up to a maximum of 10^5 iterates for all the initial conditions, the results (inner and outer upper transitions) are shown in Figure 3.27 left. The blue points, P_- to the left and P_+ to the right, correspond to the intersections with $x = 0$ of the manifolds of the vpo_L. The point P_- is the first intersection of $W^u_{\text{vpo}_L}$ with $x = 0$, and P_+ is the first intersection of $W^s_{\text{vpo}_L}$ with $x = 0$. The y coordinate of P_- is smaller than the one of P_+. In both cases we refer to the manifolds of vpo_L as seen in Σ. Compare with the section through $x = 0$ of the upper part of the blue curves in Figure 3.26. Note also that in Figure 3.27 we display $y - 1$ as horizontal coordinate, while $\dot{y}$ is used for the vertical one.

To see the behaviour when the number of iterates increases, the right part of Figure 3.27 shows the evolution when we consider iterates in the slice after a maximal number of iterations going from 10^5 to 8×10^5 and, later, to 5×10^6 (from green to blue and then to red). The points are plotted in the reverse order. So, blue points hidden red ones and green points hidden blue ones. In magenta we show the location of P_-. To prevent from too heavy files we take the narrower slice $|x| < 10^{-4}$ and only show iterates when moving in the upper part to the left, that is, upper inner transitions.

It is interesting to display statistics of the process. A simple measure is the evolution of the distance of the iterates to the point P_-, marked in magenta in Figure 3.27 right. We use the slice $|x| < 10^{-3}$ and all the Poincaré iterates (up to 5×10^6 for the 1920 initial points, except for 37 points which escape, after escape is detected). Then we compute the distances $r_{k,i}$ to P_- in the $(y, \dot{y})$ variables, where i is the index of the initial point and k the number of the Poincaré iterate. One takes samples of the $r_{k,i}$ for all the indices i and for ranges of k of the form $((j-1)M, jM]$, $j = 1, \ldots, 100$, with $M = 50,000$. The samples can be labelled by the final value of k. The Figure 3.28 displays, on the left, the behaviour of the average distance as a function of the final value of k in the range of values of k in the sample, while the behaviour of the standard deviation is shown on the right. For these computations both inner transitions (upper and lower) have been taken into account, in order to have larger samples (the total number of inner transitions amounts to 1643007).

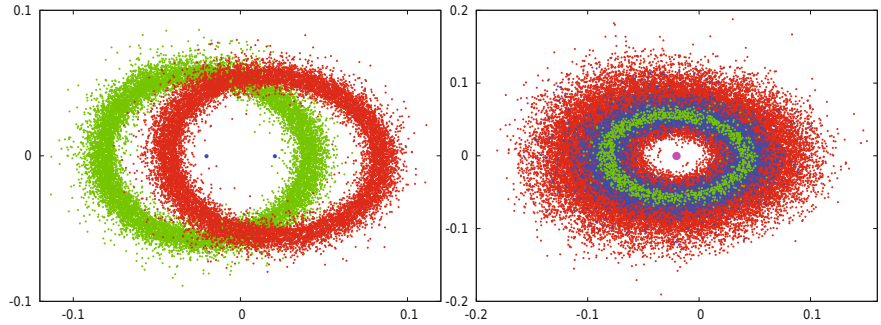

Figure 3.27: For the set of points described in the text we show the $(y-1, \dot{y})$ projections using different slices and times, for $y > 0$ (for $y < 0$ it is similar). *Left:* the slice is defined as $|x| < 10^{-3}$ and we restrict to the first 10^5 Poincaré iterates of the initial points. In green (resp., red) the points when the iterates move to the left (resp., to the right) when looking at them projected on (x, y). We also show the location of $P_{\pm}$, as described in the text. *Right:* points in the upper inner transitions. In red (resp., blue, green) we plot the points on the slice for a number of Poincaré iterates up to 5×10^6 (resp., up to 8×10^5, up to 10^5).

The results deserve some discussion. We can consider a diffusion process but, as the rate of diffusion is related to the passage from some 2D torus (invariant curve in the Poincaré section) to a nearby one, from the comments preceding Figure 3.25, the rate of diffusion is not constant. It increases going away from the vpo_L and then it decreases again when approaching the hpo_L. From the left plot in Figure 3.28 it seems that the average is still in a range where the diffusion rate is increasing. This asymmetry is what produces the increase of the average. Note that the value of the distance to P_- for the first iterates which fall in the slice has an average of ≈ 0.0597. Concerning the standard deviation, one should mention that it takes a not so small value (≈ 0.005) for $k = 50,000$ (the first displayed point). One of the reasons for this is that, looking at the green points in Figure 3.27, one checks that they are scattered around an ellipse, not a circle. Also, after 50,000 iterates the scattering is non-negligible.

One can mention that a good fit of the data for the standard deviation, as a function of the number of Poincaré iterates, k, is of the form $\sigma \approx c(a_0 + a_1 k + a_2 k^2)^{1/2}$ with $a_0, a_1 > 0$, $a_2 < 0$, and c a small positive constant. The negative character of a_2 should be due to the decrease of the diffusion rate when going to the outer curves in Figure 3.25.

Furthermore, when the distance d to P_- reaches a value d^* less than, but not too far from 0.18, the orbits quickly escape. One can check that the upper part of the unstable manifold of the hpo_L has a first intersection with $x = 0$ on a curve, similar to a circle, for which the distance to P_- takes an average value equal to 0.2. Hence, we can consider this as a diffusion process with varying diffusion rate (first increasing, later decreasing, as a function of the distance to P_-) and with

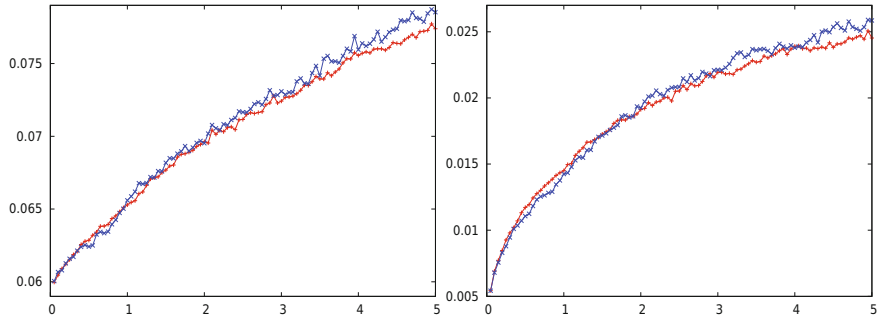

Figure 3.28: The *left* (resp., *right*) plot shows (in red) the evolution of the average (resp., standard deviation) for ranges of k of the form $((j-1)M, jM]$, $j = 1, \ldots, 100$, with $M = 50,000$. The horizontal variable in the plots refers to millions of Poincaré iterates. For comparison, the blue lines show the same results, with a reduced set of initial points, for computations done using quadruple precision. See the text for details.

an absorbing barrier: reaching $d = d^*$ the points disappear from the system.

It is worth commenting also that, as an additional check, preliminary computations concerning diffusion and the related statistics have been carried out using quadruple precision. The size of the sample of initial points has been reduced by a factor of 4. The number of escapes before reaching $N = 5 \times 10^6$ is 9, in good agreement with the previous result. Note that now the samples for the statistics are smaller, which gives slightly larger errors in the determination of average and standard deviation. For comparison, the results are displayed in blue also in Figure 3.28.

Concerning escape, the following experiment has been carried out. A total of 625 initial conditions has been taken in Σ at distances of the order of 10^{-13} from the intersection of the vpo_L with Σ. Poincaré iterates have been computed up to a maximum of 10^9. The first escape is produced after a number of iterates close to 65×10^5. Only 13 points subsist for the full 10^9 iterates, most of them spending a big part of the iterations very close to invariant tori. This is, again, related to the stickiness of these tori. A plot of the number of points which subsist after k iterations, for values of k multiples of 10^7 is shown in Figure 3.29.

Furthermore, taking initial data close to the 9 outermost tori in Figure 3.25 (again using samples of 625 points), one checks that all points escape, and that the average number of iterates for the escape decreases in an exponential way when we approach the outer torus. If the same experiment is done with 625 initial points close to the hpo_L, the result is that all of them escape. In that case, as the orbit lives in $z = 0$, one can count the number of crossings of the orbits through the section $x = 0$, either with $y > 0$ or with $y < 0$, and either with $\dot{x} > 0$ or with $\dot{x} < 0$. The average number of such crossings is 14175. Note that, in contrast with the passage of Poincaré iterates through a slice around $x = 0$, it happens that

there are outer and inner, upper and lower crossings both with $\dot{x} > 0$ and with $\dot{x} < 0$. See [48] for an explanation of this fact.

These results, displayed in Figure 3.29, require a few comments. Up to 64.9 million iterates there is no escape. Only 14 points escape before 10^8 iterates. Then, up to $\approx 3 \times 10^8$ iterates the number of subsisting points is nearly linear in the number of iterates, that is, a rate of decrease close to a constant. Finally, up to $\approx 9 \times 10^8$ the rate of escape is slightly below an exponential one. The last escape was produced around 870 million iterates. To explain these changes is a nice open problem.

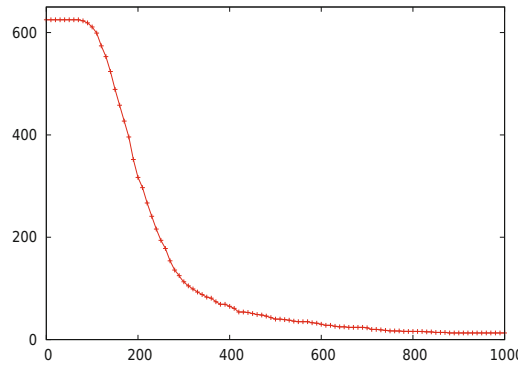

Figure 3.29: Statistics of the number of non-escaping points, starting close to the vpo_L, as a function of the number of Poincaré iterations. For the simulations one has used a sample of 625 initial points. In the horizontal axis the number of iterations is shown in millions.

A basic ingredient for this application is to have an efficient method to compute Poincaré iterates. The steps are the following:

(i) The computation, stability properties and unstable direction of the vpo_L, as fixed point of the Poincaré map, is an easy task. The invariant curves of $\mathcal{P}$ are computed by looking at a representation of the variables $(x, y, \dot{x}, \dot{y})$ as Fourier series in a parametrization angle, using a number of harmonics between 6 and 26, depending on the torus, as explained in Subsection 3.3.3. The symmetries imply that, setting the origin of the angle at the minimal value of x, both x and $\dot{y}$ are even, while y and $\dot{x}$ are odd. In this way, the left plot in Figure 3.25 has been obtained. As a side comment we remark that the rotation numbers are of the order of 10^{-4} and decreasing when going away from the vpo_L. This produces some problems in the condition number of the linear systems to be solved in the Newton iterations.

(ii) The next step is the computation of invariant unstable/stable manifolds of the invariant curves. The reversibility implies that it is enough to compute the unstable ones, the stable being then recovered by the symmetries.

We recall that the manifolds have a parametrization as a function of an angle and a distance to the curve. A fundamental domain is diffeomorphic to a cylinder. Looking for points such that after some number of iterations are on an hyperplane Π requires a continuation method (e.g., to have the starting distance as a function of the angle) or any similar device. This has been used for the right-hand plot in Figure 3.25. The plots in Figure 3.26 follow immediately from the computation of Poincaré iterates.

(iii) To produce Figure 3.27 only requires the computation of Poincaré iterates, detection of the passage through a given slice and whether an inner or outer, upper or lower passage occurs. These are elementary tasks, despite the computational cost being high. The statistics can be produced by elementary means.

Note that the difficulties mentioned in item (i), about the smallness of the rotation number, could be expected a priori. The problem in this region of the phase space is a tiny perturbation of the two-body problem in synodical coordinates. If $\mu \to 0$ the limit is the two-body problem, without the singularities which occur in the case of L_1 and L_2 due to the presence of the secondary, which lead, under suitable scaling, to a limit non-integrable case which is Hill's problem, see [35, 49]. Hence, for $\mu \to 0$, the rotation numbers of the ICs like the ones in Figure 3.25 tend to zero. Concretely they are $\mathcal{O}(\mu)$, in contrast with the hyperbolicity at L_3 and also at the ICs, the vpo_L and the hpo_L, which is $\mathcal{O}(\sqrt{\mu})$. The possible resonances are of a so high order that they become undetectable. The diffusion comes only from the effect of the heteroclinic connections of the manifolds of these ICs. The situation is more complex if there is also a relevant amount of hyperbolicity in the centre manifold itself. See related topics in [13].

Summarizing: one has good evidence of the existence of diffusion associated to the centre manifold of L_3 on levels of the Jacobi constant not too far from the value at that point. Certainly one can produce escape, due to the effect of the secondary and even for μ as small as 0.0002, but the escape time is large. Anyway, there are many topics which require further research.

Acknowledgments

Some of the topics presented in this Chapter have been partially supported by grants MTM2010-16425 and MTM2013-41168-P (Spain), 2009 SGR 67 and 2014 SGR 1145 (Catalonia). The author is grateful to the Centre de Recerca Matemàtica where he was staying during the preparation of the written version of these lectures.

Bibliography

[1] I. Baldomà and À. Haro. "One dimensional invariant manifolds of Gevrey type in real-analytic maps". *Discrete Contin. Dyn. Syst. Ser. B* **10** (2008), 295–322.

[2] X. Cabré, E. Fontich and R. de la Llave. "The parameterization method for invariant manifolds I: Manifolds associated to non-resonant subspaces". *Indiana Univ. Math. J.* **52** (2) (2003), 283–328.

[3] X. Cabré, E. Fontich and R. de la Llave. "The parameterization method for invariant manifolds II: Regularity with respect to parameters". *Indiana Univ. Math. J.* **52** (2) (2003), 329–360.

[4] X. Cabré, E. Fontich and R. de la Llave. "The parameterization method for invariant manifolds III: Overview and applications". *J. Differential Equations* **218** (2) (2005), 444–515.

[5] A. Chenciner, J. Gerver, R. Montgomery and C. Simó. "Simple Choreographic Motions of N Bodies: A Preliminary Study". In *Geometry, Mechanics and Dynamics*, P. Newton, P. Holmes, A. Weinstein, editors, pp. 287–308, Springer-Verlag, 2002.

[6] A. Chenciner and R. Montgomery. "A remarkable periodic solution of the three-body problem in the case of equal masses". *Ann. of Math.* (2) **152** (3) (2000), 881–901.

[7] B.V. Chirikov, "A universal instability of many-dimensional oscillator systems". *Phys. Rep.* **52** (5) (1979), 264–379.

[8] P.M. Cincotta, C.M. Giordano and C. Simó. "Phase space structure of multidimensional systems by means of the Mean Exponential Growth factor of Nearby Orbits". *Physica D* **182** (2003), 151–178.

[9] A. Delshams and P. Gutiérrez. "Effective stability and KAM theory". *J. Differential Equations* **128** (2) (1996), 415–490.

[10] E. Fontich and C. Simó. "The Splitting of Separatrices for Analytic Diffeomorphisms". *Ergod. Th. & Dynam. Sys.* **10** (1990), 295–318.

[11] E. Fontich and C. Simó. "Invariant Manifolds for Near Identity Differentiable Maps and Splitting of Separatrices". *Ergod. Th. & Dynam. Sys.* **10** (1990), 319–346.

[12] V. Gelfreich and C. Simó. "High-precision computations of divergent asymptotic series and homoclinic phenomena". *Discrete and Continuous Dynamical Systems B* **10** (2008), 511–536.

[13] V. Gelfreich, C. Simó and A. Vieiro. "Dynamics of $4D$ symplectic maps near a double resonance". *Physica D* **243** (2013), 92–110.

[14] A. Giorgilli, A. Delshams, E. Fontich, L. Galgani and C. Simó. "Effective stability for a Hamiltonian system near an elliptic equilibrium point, with an application to the restricted three body problem". *J. Diff. Eq.* **77** (1989), 167–198.

[15] G. Gómez, A. Jorba, J. Masdemont and C. Simó. *"Dynamics and Mission Design Near Libration Points. Volume 3: Advanced Methods for Collinear Points"*. World Sci. Pub., Monograph Ser. Math. Vol. 4, Singapore, xiv+187 pp., 2000.

[16] G. Gómez, A. Jorba, J. Masdemont and C. Simó. *"Dynamics and Mission Design Near Libration Points. Volume 4: Advanced Methods for Triangular Points"*. World Sci. Pub., Monograph Ser. Math. Vol. 5, Singapore, xii+262 pp., 2000.

[17] G. Gómez, J. Llibre, R. Martínez and C. Simó. *"Dynamics and Mission Design Near Libration Points. Volume 1: Fundamentals: The Case of Collinear Libration Points"*. World Sci. Pub., Monograph Ser. Math. Vol. 2, Singapore, xx+442 pp., 2001.

[18] G. Gómez, J. Llibre, R. Martínez and C. Simó. *"Dynamics and Mission Design Near Libration Points. Volume 2: Fundamentals: The Case of Triangular Libration Points"*. World Sci. Pub., Monograph Ser. Math. Vol. 3, Singapore, xii+146 pp., 2001.

[19] J.M. Greene, "A method for determining stochastic transition". *J. Math. Phys.* **6** (20) (1976), 1183–1201.

[20] M. Hénon, "Numerical study of quadratic area-preserving mappings". *Quart. Appl. Math.* **27** (1969), 291–312.

[21] M. Hénon and C. Heiles. "The applicability of the third integral of motion: Some numerical experiments". *Astronomical J.* **69** (1964), 73–79.

[22] À. Jorba and Maorong Zou. "A software package for the numerical integration of ODE's by means of high-order Taylor methods". *Experiment. Math.* **14** (1) (2005), 99–117.

[23] À. Jorba and E. Olmedo. "On the computation of reducible invariant tori on a parallel computer". *SIAM J. Appl. Dyn. Syst.* **8** (4) (2009), 1382–1404.

[24] T. Kapela and C. Simó. "Computer assisted proofs for nonsymmetric planar choreographies and for stability of the Eight". *Nonlinearity* **20** (2007), 1241–1255.

[25] F. Ledrappier, M. Shub, C. Simó and A. Wilkinson. "Random versus deterministic exponents in a rich family of diffeomorphisms". *J. Stat Phys.* **113** (2003), 85–149.

[26] R.S. MacKay. "A renormalisation approach to invariant circles in area-preserving maps". *Physica D* **7** (1-3) (1983), 283–300.

[27] R.S. MacKay. *"Renormalisation in area-preserving maps"*. Advanced Series in Nonlinear Dynamics, 6. World Scientific. 1992.

[28] R. Martínez and C. Simó. "The invariant manifolds at infinity of the RTBP and the boundaries of bounded motion". *Regular and Chaotic Dynamics* **19** (2014), 745–765.

[29] J. Mather. "Minimal measures". *Comment. Math. Helv.* **64** (1989), 375–394.

[30] J. Mather. "Action minimizing invariant measures for positive definite Lagrangian systems". *Math. Z.* **207** (1991), 169–207.

[31] R. McGehee. "A stable manifold theorem for degenerate fixed points with applications to Celestial Mechanics". *J. Differential Equations* **14** (1973), 70–88.

[32] N. Miguel, C. Simó and A. Vieiro. "On the effect of islands in the diffusive properties of the standard map, for large parameter values". *Foundations of Computational Mathematics* **15** (2014), 89–123.

[33] C. Moore. "Braids in Classical Gravity". *Physical Review Letters* **70**, (1993), 3675–3679.

[34] J.J. Morales, J.P. Ramis and C. Simó. "Integrability of Hamiltonian Systems and Differential Galois Groups of Higher Variational Equations". *Annales Sci. de l'ENS* 4^e série **40** (2007), 845–884.

[35] J.J. Morales, C. Simó and S. Simón. "Algebraic proof of the non-integrability of Hill's Problem". *Ergodic Theory and Dynamical Systems* **25** (2005), 1237–1256.

[36] A. Neishtadt, "The separation of motions in systems with rapidly rotating phase". *J. Appl. Math. Mech.* **48** (1984), 133–139.

[37] N.N. Nekhorosev, "An exponential estimate of the time of stability of nearly-integrable Hamiltonian systems". *Russian Mathematical Surveys* **32** (6) (1977), 1–65.

[38] A. Olvera and C. Simó. "An obstruction method for the destruction of invariant curves". *Physica D* **26** (1987), 181–192.

[39] J. Sánchez, M. Net and C. Simó. "Computation of invariant tori by Newton–Krylov methods in large-scale dissipative systems". *Physica D* **239** (2010), 123–133.

[40] C. Simó. "Analytical and numerical computation of invariant manifolds". In *"Modern methods in Celestial Mechanics"*, D. Benest and C. Froeschlé, editors, pp. 285–330, Editions Frontières, 1990.

[41] C. Simó. "Averaging under fast quasiperiodic forcing". In Proceedings of the NATO-ARW *"Integrable and chaotic behaviour in Hamiltonian Systems"* (Torun, Poland, 1993), I. Seimenis, editor, pp. 13–34, Plenum Pub. Co., New York, 1994.

[42] C. Simó. "Effective Computations in Celestial Mechanics and Astrodynamics". In *"Modern Methods of Analytical Mechanics and their Applications"*, V.V. Rumyantsev and A.V. Karapetyan, editors, CISM Courses and Lectures **387**, 55–102, Springer, 1998.

[43] C. Simó. "Invariant Curves of Perturbations of Non Twist Integrable Area Preserving Maps". *Regular and Chaotic Dynamics* **3** (1998), 180–195.

[44] C. Simó. "Dynamical properties of the figure eight solution of the three-body problem". In *"Proceedings of the Celestial Mechanics Conference dedicated to D. Saari for his 60th birthday"* (Evanston, 1999), A. Chenciner et al., editors, *Contemporary Mathematics* **292** (2000), 209–228.

[45] C. Simó. "New families of Solutions in N–Body Problems". In *"Proceedings of the 3-rd European Congress of Mathematics"*, C. Casacuberta, R. M. Miró-Roig, J. Verdera, S. Xambó, editors, *Progress in Mathematics series* **201** (2001), 101–115 (Birkäuser, Basel).

[46] C. Simó. "Some properties of the global behaviour of conservative low dimensional systems". In *"Foundations of Computational Mathematics"* (Hong Kong, 2008), F. Cucker et al. editors, pp. 163–189, London Math. Soc. Lecture Notes Series **363**, Cambridge Univ. Press, 2009.

[47] C. Simó. "Measuring the total amount of chaos in some Hamiltonian Systems". *Discrete and Continuous Dynamical Systems A* **34** (2014), 5135–5164.

[48] C. Simó, P. Sousa-Silva and M. Terra. "Practical Stability Domains near $L_{4,5}$ in the Restricted Three-Body Problem: Some preliminary facts". In *Progress and Challenges in Dynamical Systems* **54** (2013), 367–382.

[49] C. Simó and T. Stuchi. "Central Stable/Unstable Manifolds and the destruction of KAM tori in the planar Hill problem". *Physica D* **140** (2000), 1–32.

[50] C. Simó and D. Treschev. "Stability islands in the vicinity of separatrices of near-integrable symplectic maps". *Discrete and Continuous Dynamical Systems B* **10** (2008), 681–698.

[51] C. Simó and C. Valls. "A formal approximation of the splitting of separatrices in the classical Arnold's example of diffusion with two equal parameters", *Nonlinearity* **14** (2001), 1707–1760.

[52] C. Simó and A. Vieiro. "Resonant zones, inner and outer splittings in generic and low order resonances of Area Preserving Maps". *Nonlinearity* **22** (2009), 1191–1245.

[53] C. Simó and A. Vieiro. "Dynamics in chaotic zones of area preserving maps: close to separatrix and global instability zones". *Physica D* **240** (2011), 732–753.

Some classical books:

- V.I. Arnold. *"Les méthodes mathématiques de la mécanique classique"*. Éditions Mir, Moscow, 1976.
- V.I. Arnold and A. Avez. *"Problèmes ergodiques de la mécanique classique"*. Gauthier-Villars, Paris 1967.
- M.W. Hirsch, C.C. Pugh and M. Shub. *"Invariant Manifolds"*. Lecture Notes in Mathematics **583**, Springer-Verlag, Heidelberg, 1977.
- J.K. Moser. *"Stable and random motions in Dynamical Systems: with special emphasis on Celestial Mechanics"*, Princeton University Press, Princeton, 1973.
- C.L. Siegel and J.K. Moser. *"Lectures on Celestial Mechanics"*. Die Grundlehren der mathematischen Wissenschaften, Band 187. Springer-Verlag, New York-Heidelberg, 1971.

Slides of several talks:

(A) *"Taylor method for the integration of ODE"*, number 8.
http://www.maia.ub.es/dsg/2007/.

(B) *"Some properties of the global behaviour of conservative low dimensional systems"*, number 3.
http://www.maia.ub.es/dsg/2008/.

(C) *"On the role of Dynamical Systems in Celestial Mechanics"*, number 4.
http://www.maia.ub.es/dsg/2010/.

(D) *"Domains of Practical Stability near $L_{4,5}$ in the 3D Restricted Three-Body Problem"*, number 8.
http://www.maia.ub.es/dsg/2012/.

(E) *"Quadratic Area Preserving Maps in R^2"*, number 5.
http://www.maia.ub.es/dsg/2013/.

(F) *"The dances of the N bodies"*, number 7.
http://www.maia.ub.es/dsg/2013/.

(G) *"The role of Michel Hénon in detecting regular and chaotic dynamics in conservative systems"*, number 8.
http://www.maia.ub.es/dsg/2013/.

(H) *"Measure of the chaotic domain in simple Hamiltonian systems"*, number 7.
http://www.maia.ub.es/dsg/2014/.

(I) *"Splitting, return maps and confined motion in the planar RTBP: Theory and praxis"*, number 1.
http://www.maia.ub.es/dsg/2015/.

(J) *"Experiments looking for theoretical predictions"*, number 2.
http://www.maia.ub.es/dsg/2015/.